Multifunctional and sustainable vitrimer systems for self-healing, scratch resistance, and corrosion protection

Journal of Industrial and Engineering Chemistry 162 (2026) 454–469

Contents lists available at ScienceDirect

Journal of Industrial and Engineering Chemistry

journal homepage: www.elsevier.com/locate/jiec

Full Length Article

Multifunctional and sustainable vitrimer systems for self-healing, scratch resistance, and corrosion protection

Anna Liguori [a,1,*], Luigi Gamberini [a,1], Leonardo Iannucci [b], Carlo Gotti [c], Mattia Bartoli [d], Federica Rizzi [e,f], Andrea Zucchelli [c,g], Maria Lucia Curri [e,f,h], Sabrina Grassini [b], Giulio Malucelli [i,*], Maria Letizia Focarete [a,j]

[a] Department of Chemistry "Giacomo Ciamician" and INSTM UdR of Bologna, University of Bologna, via P. Gobetti 85, Bologna 40129, Italy
[b] Department of Applied Science and Technology, Politecnico di Torino, Corso Duca degli Abruzzi 24, Turin 10129, Italy
[c] Advanced Mechanics and Materials, Interdepartmental Center for Industrial Research (CIRI-MAM), University of Bologna, Viale Risorgimento 2, Bologna 40136, Italy
[d] Istituto Italiano di tecnologia - Center for Sustainable Future Technologies, Via Livorno 60, 10144 Torino, Italy
[e] Institute for Chemical and Physical Processes, CNR-IPCF SS Bari, Via Orabona 4, 70126 Bari, Italy
[f] National Interuniversity Consortium of Materials Science and Technology (INSTM), Bari Research Unit, Via Orabona 4, 70126 Bari, Italy
[g] Department of Industrial Engineering, University of Bologna, Viale del Risorgimento, Bologna 40136, Italy
[h] Department of Chemistry, University of Bari, Via Orabona 4, 70126 Bari, Italy
[i] Department of Applied Science and Technology, Politecnico di Torino, Viale Teresa Michel 5, Alessandria 15121, Italy
[j] Health Sciences & Technologies (HST) CIRI, University of Bologna, Via Tolara di Sopra 41/E, Ozzano Emilia, 40064, Italy

ARTICLE INFO

Keywords:
Multifunctional sustainable vitrimers
Functionalized silica nanoparticles
Self-healing
Scratch resistance
Corrosion protection
Adhesion

ABSTRACT

Bio-based covalent adaptable networks represent a promising platform for the development of sustainable protective coatings combining durability, self-healing, and end-of-life management. In this work, we report a solvent-free, photocurable vitrimeric system based on bio-derived building blocks incorporating dynamic imine bonds, enabling intrinsic self-healing. The resin, synthesized from methacrylated vanillin and a flexible diamine, and diluted with methacrylated eugenol, was UV-cured in the presence of functionalized silica nanoparticles to form crosslinked composite networks in which the nanoparticles were covalently integrated. The resulting composite systems displayed homogeneous nanoparticle dispersion and tunable properties as a function of filler content. Notably, the incorporation of 2% w/w functionalized silica nanoparticles enabled complete healing in less than five minutes at temperatures as low as 80 °C without external pressure, while simultaneously imparting enhanced scratch resistance. When applied as coatings on steel substrates, pull-off adhesion tests revealed high adhesion strength for all formulations, with no evidence of coating-substrate interfacial failure. Electrochemical impedance spectroscopy measurements showed that pristine coatings provided excellent corrosion protection on steel substrates, maintaining impedance moduli above 10^7 Ω cm^2 after prolonged exposure to saline environments, whereas higher nanoparticle loadings reduced the barrier performance due to increased water uptake. Importantly, the coatings were fully removed from substrates in a diamine solution by exploiting transimination reactions of imine functionalities with diamines, allowing recovery of oligomeric fragments and clean substrate regeneration.

Introduction

Organic coatings encompass thin polymeric layers physically or chemically anchored to a bulk substrate to impart specific functionalities. These coatings often consist of thermosetting matrices combined with fillers to achieve the performance required in demanding applications [1–3]. Thermosets are particularly attractive due to their crosslinked architecture, which confers superior resistance to chemicals, solvents, and mechanical stresses compared to thermoplastic counterparts. However, as reported by van Benthem et al. [4], thermoset coatings remain susceptible to damage across multiple length scales, from macroscopic rupture and delamination to microcracking and

* Corresponding authors.
E-mail addresses: anna.liguori@unibo.it (A. Liguori), giulio.malucelli@polito.it (G. Malucelli).
[1] These authors contributed equally.

https://doi.org/10.1016/j.jiec.2026.04.045
Received 24 March 2026; Received in revised form 23 April 2026; Accepted 25 April 2026
Available online 8 May 2026

crazing, down to molecular-level bond scission. Such defects compromise the coating's protective performance, shorten the service life of the coated object, and increase maintenance costs [5].

To address these limitations, considerable effort over the past decades has been devoted to designing thermoset materials with self-healing capabilities. While early systems relied on extrinsic approaches [6], research has increasingly shifted toward intrinsic self-healing, where restoration of damaged interfaces occurs through the activation of specific dynamic and supramolecular bonds within the polymer structure [1,7–11]. Dynamic covalent chemistry has played a central role in this development. A pioneering contribution in the field was offered in 2002 by the Wudl group [12], which demonstrated heat-healable networks crosslinked by reversible Diels-Alder adducts. This polymer behaved as a rigid plastic at room temperature but transitioned to a rubbery state at 120 °C, where enhanced chain mobility and adduct dissociation enabled efficient healing. Since then, a broad variety of dynamic covalent chemistries has been implemented for thermally triggered self-healing systems, as reviewed by Zheng et al [13].

In particular, Lu et al. reported that transition-metal-catalyzed olefin metathesis is an effective route for healing cross-linked polybutadiene networks by exchanging carbon–carbon double bonds activated by a low concentration of Grubbs' second-generation catalyst [14]. Zhang et al. developed stiff polyurethanes capable of autonomous intrinsic self-healing by incorporating alkoxyamine units and a soft, highly crystalline segment with sub-ambient T_g into the polymer backbone [15]. More recently, dynamic covalent bonds have also been investigated for the design of protective coatings. Van Lijsebetten et al. synthesized vitrimeric epoxy coatings using dynamic amine-acetoacetate curing agents and demonstrated the recovery of barrier properties by monitoring scratch disappearance after thermal activation at 160 °C under pressure [16]. Very recently, Li et al. reported a PDMS-based dynamic covalent network containing reversible imine and Zn^{2+} coordination bonds, enabling autonomous self-healing and anticorrosion performance due to the inherently low T_g of PDMS [17].

Wang et al. [18] demonstrated the self-healing ability, together with the anti-corrosion properties of cardanol/furfurylamine-based polybenzoxazine vitrimeric systems containing dynamic disulfide bonds and cured with bis(4-aminophenyl) disulfide. In particular, the scratches on the coatings could self-heal after heating at 120 °C for up to 1 h. Besides, the impedance modulus values at low frequency ($|Z|_{0.01Hz}$) of the obtained coatings exceeded 10^7 Ω cm^2 after soaking in a 3.5% w/w NaCl solution for 15 days, indicating anti-corrosion properties. Yang et al. [19] synthesized an amine curing agent containing imine bonds using a polyether amine and bio-based vanillin. The curing agent was then combined with modified graphene oxide and an epoxy resin to produce composite coatings that exhibited excellent stress relaxation properties, enabling physical restoration at 190 °C and 20 MPa with a recovery rate exceeding 89%. Besides, the coatings showed outstanding aging resistance for 40 days and anti-corrosion behavior for 100 days. Shahali et al. [20] developed aromatic thermosetting vitrimeric copolyesters as self-healing and corrosion-resistant coatings for carbon steel via a condensation polymerization reaction between acetoxy functional group oligomers and carboxylic acid. After exposure to 3.5% w/w NaCl, 6 M KOH, and 1 M H_2SO_4 for 30 days, the scratched vitrimeric coatings exhibited interesting self-healing capabilities through IR heating. Besides, the deepest scratches showed significant improvement after two IR cycles.

Motivated by these advances, this work explores a solventless, bio-based photocurable resin incorporating imine functionalities to develop intrinsically self-healing protective vitrimeric systems. The presence of dynamic imine bonds, along with the aromatic character of the building blocks, provides the coatings with efficient self-healing behavior upon heating at atmospheric pressure, and promising anti-corrosion performance. To further enhance the functional response, the resin was combined with silica nanoparticles (SiNPs), which were specifically functionalized to promote their homogeneous dispersion and covalent integration into the network. This allowed us to investigate their influence on both self-healing and anticorrosion behavior. In particular, the presence of silica nanoparticles at a concentration of 2% w/w relative to the resin was found to accelerate scratch reclosure, enabling healing even at lower temperatures compared to the unfilled coating. In terms of anticorrosion properties, the pristine samples exhibited the most promising performance, showing a high impedance modulus throughout the test, which was carried out by placing the coating in contact with a 3.5% w/w NaCl aqueous electrolyte for 336 h. A progressive decrease in performance was observed with increasing SiNPs content, attributed to enhanced water uptake. Importantly, the incorporation of functionalized SiNPs imparted significant scratch resistance, a property not observed in the unfilled vitrimeric systems and directly arising from the mechanical reinforcement provided by the filler particles.

Finally, we demonstrate that the vitrimeric systems can be chemically removed from the substrate through dynamic imine exchange with a diamine reagent, enabling complete delamination and recovery of oligomeric fragments. This recyclability feature highlights the potential of these systems for developing more sustainable protective coating technologies.

Experimental section

Materials

Vanillin (VL, >99%) and 2,2′-(Ethylenedioxy)bis(ethylamine) (DOM, 99%) were purchased from BLDpharm and used without any additional purification. 3-(aminopropyl)-triethoxysilane (APTES, >98%) was purchased from TCI Chemicals. Methacrylic anhydride (94%), eugenol (4%), 4-dimethylaminopyridine (DMAP, 99%), sodium hydrogen carbonate (for analysis), sodium hydroxide (98%), sodium sulfate (≥99%), silica (fumed, d = 0.007 μm), ethylenediamine (>99%), methanol (MeOH, ≥99%), ethanol (EtOH, 97%), ethyl acetate (≥99%) and dichloromethane (DCM, ≥99%) were purchased from Sigma-Aldrich and used as received. 2-Hydroxy-2-methyl-1-phenylpropanone (Irgacure 1173), used as photoinitiator, was kindly supplied by IGM Resins Italia (Mortara (PV), Italy). Microscope glass slides from Apta Slides were used as glass supports. For adhesion strength tests, cylindrical supports (d = 20 mm, h = 10 mm) were made from a S235JR hot rolled non-alloy structural steel plate, while the substrates for corrosion tests were the CXC-35 Corrosion Coupons (purchased from Q-Lab); they are 76 × 127 × 0.8 mm^3 panels made from SAE1008 commercial-grade, cold-rolled carbon steel.

Synthesis of DOM-MVL

The CAN resin, DOM-MVL, was synthesized according to a double-step procedure consisting of the methacrylation of VL to produce methacrylated vanillin (MVL) and the subsequent Schiff-base reaction between MVL and DOM. MVL was obtained according to the previously reported procedure [21]. Briefly, VL (30.00 g, 197.17 mmol) was mixed with MAA (30.36 g, 197.00 mmol) and DMAP (0.17 g, 1.39 mmol) in a 250 mL round-bottom flask and kept under stirring at 60 °C for 24 h. The reaction product was diluted with DCM and subsequently washed with saturated aqueous sodium hydrogen carbonate, 0.5 M NaOH, 1 M NaOH, and distilled water. The organic phase was dried over Na_2SO_4, concentrated at reduced pressure, and dried under vacuum at room temperature for 2 days, yielding MVL as a white powder (81% reaction yield). The DOM-MVL resin was obtained by subjecting the MVL to a Schiff-base reaction with DOM [22,23]. In brief, MVL (4.05 g, 18.40 mmol) and DOM (1.78 g, 12.00 mmol) were placed in a 250 mL round-bottom flask and dissolved in 60 mL of DCM. The reaction was carried out at room temperature for 5 h under stirring. Afterward, the reaction mixture was subjected to the same washing and drying procedures as described for methacrylation, yielding DOM-MVL as a pale-yellow oil (96% reaction yield).

Synthesis of MEu

For the synthesis of the reactive diluent (i.e., methacrylated eugenol, MEu), eugenol (30.00 g, 182.7 mmol) was mixed with MA (29.03 g, 188.34 mmol) and DMAP (0.223 g, 5.48 mmol) in a 250 mL round-bottom flask and stirred at 45 °C for 24 h. Afterward, the reaction mixture was subjected to the same work-up procedure as described for vanillin methacrylation, yielding MEu as a pale-yellow oil (88% reaction yield) [24].

Synthesis of SB-NPs

As the first step, NH_2-NPs were obtained through a sol–gel reaction between SiNPs and APTES. Fumed silica (250 mg) was loaded inside a 500 mL round-bottom flask with 250 mL of a 95:5 w/w solution of EtOH/H_2O. The flask was sonicated for 2 h at room temperature. Then, APTES (400 mg, 1.8 mmol) was added to the flask, and the mixture was stirred at 75 °C for 2 h. The suspension was centrifuged at 6000 rpm for 2 h, and the precipitated solid was freeze-dried for 24 h, yielding a white powder. SB-NPs (350 mg) were placed in a 500 mL round-bottom flask, and ethyl acetate (350 mL) was added. The suspension was sonicated for 2 h. Then, MVL (668.18 mg, 3.04 mmol) was loaded, and the mixture was stirred for 2 h at room temperature. Then the suspension was centrifuged (6000 rpm, 20 min), and the precipitate, a pale-yellow powder, was collected and dried under vacuum overnight.

Preparation of free-standing networks and coatings

DOM-MVL:MEu resin was prepared by mixing the two components at a 50:50 wt ratio. Three formulations were produced, namely: (i) the neat resin (without nanoparticles), and (ii) composite resins containing SB-NPs at either 2% w/w or 5% w/w, calculated with respect to the total resin weight. Irgacure 1173 was then added at 4% w/w relative to the weight of the resin. Free-standing films were obtained by UV-curing the formulations according to the following procedure: first, the liquid mixtures were coated on 10x10 cm^2 glass slides using a wire-wound applicator (nominal thickness: 200 μm). Then, the coated slides were UV-cured using a Heraeus Noblelight F300S UV lamp system operating in static mode. The liquid mixtures underwent three non-consecutive exposures to UV radiation, each for 30 s; finally, the cured coatings were peeled off from the glass slides. For the preparation of coatings, the same three formulations were deposited onto glass or steel substrates and subjected to the identical curing procedure used for the free-standing films. Samples obtained from the formulation without SB-NPs were labeled ‘pristine’, whereas the composites were labeled ‘2% w/w SB-NPs’ and ‘5% w/w SB-NPs’, respectively, according to the nanoparticle loading.

Characterization of resin, nanoparticles, and free-standing networks

The chemical structures of DOM-MVL and MEu were confirmed by means of ^1H NMR spectroscopy performed on an Avance 600 (Bruker) spectrometer (600 MHz) equipped with a 5.0 mm multi-nuclear observe probe with Z-gradient. $CDCl_3$ was used as both the solvent and the internal standard for chemical shift calibration.

The chemical structures of functionalized NPs, free-standing networks, and oligomers derived from coating decomposition were investigated using ATR-FTIR with an ALPHA II PLATINUM-ATR (Bruke Corporation). All the spectra were recorded in the wavenumber range of 4000 − 400 cm^{-1} using 48 scans at a resolution of 4 cm^{-1}.

The thermogravimetric behavior of NH_2-NPs and SB-NPs, as well as of the free-standing films, was investigated by means of a TGA Q500 (TA-Instruments). Samples with a weight of around 5–10 mg were subjected to a heating scan from room temperature to 700 °C with a heating rate of 10 °C/min in an air atmosphere. Differential scanning calorimetry (DSC) analysis of the films was performed using a DSC Q2000 instrument (TA Instruments) equipped with a refrigerated cooling system (RCS) in N_2 atmosphere. 5–10 mg of sample was sealed in an aluminum crucible and subjected to a heating scan from −90 °C to 150 °C with a heating rate of 20 °C/min. Tg was taken as the half-height of the glass transition heat capacity step. Stress relaxation analyses were performed using a DMA Q800 (TA Instruments). The measurements were performed in a custom stress relaxation mode with a static force of 0.01 N, at a frequency of 1.0 Hz. The Poisson’s ratio was 0.44. The samples were first heated to 60 °C and equilibrated for 5 min; after that, a constant 2% strain was applied, and the relaxation modulus and stress were recorded over time.

The efficiency of NPs' surface functionalization was evaluated using the ninhydrin assay, a well-established colorimetric method for the quantitative determination of primary amine groups [25]. Briefly, the ninhydrin reagent was prepared by dissolving 110 mg of ninhydrin in 16 mL of ethanol (0.68% w/v), followed by the addition of 4 mL of 2,6-lutidine. A calibration curve was first generated by reacting an excess of ninhydrin solution with APTES standard solutions in the concentration range of 0.0225–0.375 mM. Upon heating at 90 °C for 5 min in a thermostated bath, the reaction between ninhydrin and amine (–NH_2) groups produced a color change from pale yellow to deep blue, due to the formation of Ruhemann’s Blue. The characteristic absorption band of this chromophore at 582 nm was monitored by UV–vis spectroscopy and employed for constructing the calibration plot and determining the corresponding extinction coefficient. For the analysis of functionalized NPs, 25 μL of the APTES-MSNs suspension collected after the grafting reaction was mixed with 975 μL of ninhydrin solution (3×10^{-2} M). The mixture was heated at 90 °C for 5 min, resulting in the development of blue coloration associated with surface amino groups. Then, the absorbance measured at 582 nm was used to quantify the amount of –NH_2 functionalities present on the NPs surface. Transmission electron microscopy (TEM) analysis was performed by using a JEM1011 instrument (JEOL, Akishima, Tokyo, Japan) operating at an accelerating voltage of 100 keV and equipped with a high-resolution CCD camera. Samples were deposited from ethanol onto carbon-coated copper grids and allowed to dry prior to imaging. Dynamic light scattering (DLS) and ζ-potential measurements were carried out using a Zetasizer nano ZSP (Malvern, Worcestershire, UK) equipped with a 50 mW laser diode operating at 532 nm. These analyses were employed to determine the mean hydrodynamic diameter (reported as intensity-weighted mean), polydispersity index (PDI), and ζ-potential of the NPs [26]. Data are reported as mean ± standard deviation from three independent measurements.

Gel content measurements were carried out to investigate the solvent resistance of the free-standing films by immersing each sample (around 30 mg) in 3 mL of DCM for 72 h at room temperature. After being removed from the solvent, the samples were dried in a vacuum oven at 60 °C until a constant weight was reached. The gel fraction was determined according to equation (1).

$$Gel\ content\% = \frac{m_f}{m_i} x100 \quad (1)$$

where m_f is the final weight of the sample after 72 h of immersion, m_i is the weight before the immersion. The analysis was performed in triplicate.

Characterization of coatings

Atomic force microscopy (AFM) measurements were carried out in ambient conditions using a Bruker Innova microscope in tapping mode, with commercial silicon tips having a nominal resonance frequency of 300 kHz (TAP300Al-G). Image analysis and post-processing were performed using Gwyddion software [27].

Scanning Electron Microscopy (SEM) analyses were performed using a Zeiss Supra 40 FESEM by Zeiss. The samples were analysed using an

accelerating voltage of 5 kV and an aperture size of 30 μm. To ensure conductivity, a thin (about 12 nm) layer of platinum was coated on the samples using the Quorum Q150TS Sputter Coater. The coater was operated at 30 mA for 20 s in an argon atmosphere. The self-healing properties of the coatings applied on both glass and steel substrates were investigated at different temperatures, i.e. 120 °C, 100 °C, and 80 °C. A controlled scratch was made on the coating surface with a blade. Care was taken to ensure that the scratch remained within the coating. Then, the damaged samples were allowed to heal at the selected temperature by placing the coated substrate on a pre-heated hot plate. For coatings deposited on glass substrates, the multiple-cycle self-healing behavior was evaluated at 120 °C, as all the coatings exhibited complete scratch reclosure at this temperature. Three consecutive scratches were applied sequentially. Each new scratch was applied only after the previous one had completely closed. The repair process was monitored using a Dino-Lite camera (magnification 40x).

The anti-scratch properties were investigated in accordance with ASTM D3363–22. 6H Pencil lead (diameter 1 mm) with defined geometry was pushed over the coated glasses at an angle of 45° and a speed of 30 mm/s. The possible scratch formation was investigated using an optical microscope (Zeiss Axiocam 208) equipped with ZEN 3.6 software.

The adhesion strength of the coating formulations (Pristine, 2% w/w SB-NPs, and 5% w/w SB-NPs) on S235JR steel was evaluated via pull-off tests in accordance with the EN ISO 4624 standard [28]. The substrates for the coatings consisted of cylindrical specimens (diameter = 20 mm, thickness = 10 mm) machined from S235JR structural steel using Electrical Discharge Machining (EDM) to ensure dimensional precision. A threaded M6 hole was drilled into the back face of each cylinder to facilitate coupling with the testing machine. Prior to coating application, the test surfaces were subjected to abrasive blasting (sandblasting) to enhance mechanical interlocking and remove surface contaminants. 3 cylinders were coated for each formulation. As shown in the test setup reported in the Results and Discussion section, an uncoated cylinder of the same geometry (dolly) was glued to each coated sample after applying three drops of commercial cyanoacrylate adhesive (UHU, Rotterdam, The Netherlands), characterized by a nominal tensile strength of 12 MPa. To ensure perfect coaxial alignment during bonding and minimize bending moments, a custom-designed PTFE fixture was employed. A constant contact pressure of about 10 kPa was maintained during the curing phase (24 h at room temperature, as per manufacturer specifications). The excess adhesive was properly removed from the joint perimeter before curing. Pull-off tests were conducted using a servo-hydraulic testing system (Instron Systems, Model 8033) equipped with a 20 kN load cell. The load was applied perpendicular to the substrate plane under force control at a constant rate of 44 N/s, calculated to induce failure within 90 s, as prescribed by the ISO standard. To ensure uniaxial loading and eliminate bending moment, the assembly was connected to the machine actuators using self-aligning spherical joints. Machine compliance was characterized prior to testing and subtracted from the displacement data to isolate the assembly response. After failure, the fracture surfaces were analyzed to determine the locus of failure. High-resolution optical images of both the substrate and dolly sides were processed using Fiji software [29] to quantify the percentage area of each failure mode. Failure types were classified as follows: cohesive failure occurring within the coating layer (**CC**); adhesive failure at the glue-coating interface (**GC**); and adhesive failure at the coating-substrate interface (**CS**).

The corrosion protection effectiveness of the coatings was assessed using electrochemical impedance spectroscopy (EIS) measurements. Samples were tested in a conventional 'coating cell' in a 3-electrode configuration, where the coated steel was the working electrode, a graphite rod the counter electrode and an Ag/AgCl electrode was used as reference. The electrolyte was a 3.5% w/w NaCl aerated solution, and all measurements were acquired at room temperature. EIS measurements were performed using the Palmsens4 potentiostat, applying a 10 mV sinusoidal signal in the frequency range from 10^5 Hz to 10^{-2} Hz (10 points per frequency decade). After immersion in the electrolyte, EIS measurements were acquired every 24 h up to 336 h. The working electrode area was about 12.56 cm^2, and all tests were performed in triplicate to ensure reproducibility.

The possibility of decomposing the coatings and removing them from the substrates was also demonstrated. Glass substrates (2 cm x 3 cm) coated with pristine or 5% w/w SB-NPs films were immersed in 5 mL ethylenediamine and heated at 60 °C for 30 min. Then, the glass was removed and a dark orange solid precipitate was collected, dried under vacuum overnight, and subsequently characterized through ATR-FTIR. The recovered oligomeric fragments were subsequently used to prepare recycled free-standing films according to the following procedure. For the pristine system, 100 mg of oligomeric solid were mixed with 10 mg of MVL and 5 mg of Irgacure 2959 by grinding. The resulting powder was placed in a Teflon mold and hot-pressed at 100 °C for 10 min under 20 bar. For the 5% w/w SB-NPs system, 100 mg of oligomeric solid were mixed with 10 mg of MVL, 5 mg of SB-NPs, and 5 mg of Irgacure 2959 by grinding. The mixture was then placed in a Teflon mold and hot-pressed under the same conditions. The recycled films were finally characterized by ATR-FTIR and TGA.

Results and discussion

The reactions involved in the synthesis of the resin are illustrated in **Fig. S1**. The preparation of DOM-MVL begins with the methacrylation of the phenolic group of vanillin using methacrylic anhydride, followed by a Schiff-base reaction between its aldehyde group and DOM [22,30].

EuMet, obtained through the methacrylation of eugenol, was used as a reactive diluent and substitute of organic solvents, due to its high miscibility with DOM-MVL [24]. The presence of a vinyl group in its structure favors its covalent incorporation into the thermoset structures. The successful synthesis of both resin components was confirmed via ^{1}H NMR analysis (**Fig. S2**).

Commercial SiNPs were surface-functionalized to enhance dispersion in the resin and to promote covalent immobilization in the resulting network. The functionalization procedure consists of two steps, schematically summarized in Fig. 1a. First, a sol–gel reaction between the hydroxyl groups on the SiNPs surface and APTES yields amino-terminated nanoparticles (NH_2-NPs). In the subsequent step, these terminal amine groups undergo a Schiff-base reaction with MVL, leading to the formation of SB-NPs.

The resin and the SB-NPs, at concentrations of 2% w/w and 5% w/w relative to the total resin weight, were mixed together in the presence of the photoinitiator and subsequently UV-cured, yielding CAN-based composites in which the SB-NPs were covalently integrated, as schematized in Fig. 1b. The imine linkages within the network imparted a vitrimeric behavior to the resulting CAN. Prior to resin curing, the commercial SiNPs and the nanoparticles obtained after each functionalization step were thoroughly characterized.

Characterization of functionalized nanoparticles

The morphology, surface chemistry, and colloidal properties of the functionalized silica nanoparticles were comprehensively evaluated; the results are reported in Fig. 2. Transmission electron microscopy (TEM) analysis was performed to assess particle morphology and size before and after surface functionalization. As illustrated in Fig. 2 **a–c**, all samples consist of nanosized, roughly spherical particles that appear strongly aggregated into irregular clusters. This aggregation prevented clear resolution of individual NPs, resulting in compact assemblies rather than isolated objects. Nevertheless, statistical TEM analysis reveals that the aggregates are composed of nanosized building blocks, with average particle diameter of 9 ± 2 nm for pristine NPs, 11 ± 3 nm for NH_2-NPs, and 13 ± 2 nm for SB-NPs. The modest but progressive increase in particle size confirms the successful stepwise

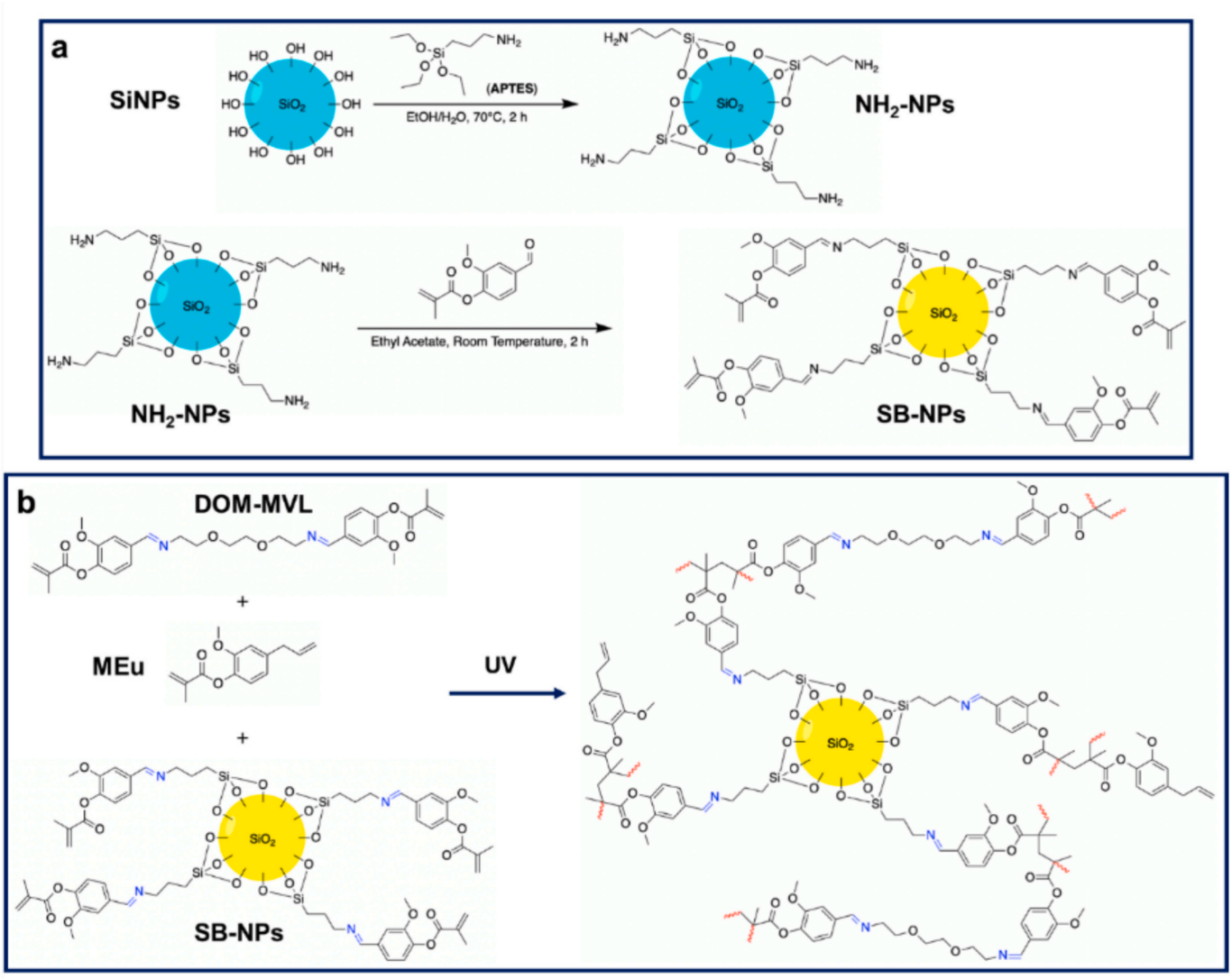

Fig. 1. Scheme of a) SiNPs functionalization, b) chemical structure of composite vitrimer deriving from the curing reaction between the resin and SB-NPs.

functionalization of the silica surface.

The presence and relative abundance of primary amine groups on the NPs surface were quantified using the ninhydrin assay (Fig. 2d). Ninhydrin reacts selectively with –NH_2 groups to form the deep blue Ruhemann's blue chromophore, whose intensity is proportional to the amine content. NH_2-NPs (red dotted line) exhibited a markedly higher absorbance than pristine NPs (black dotted line), confirming efficient amine grafting. Subsequent functionalization to produce SB-NPs (blue dotted line) led to a reduced but detectable ninhydrin response, indicating partial consumption or masking of –NH_2 groups. Quantitatively, the amino group concentrations were $1.3{\cdot}10^{-7}$ mol NH_2/mg NPs and $2{\cdot}10^{-8}$ mol NH_2/mg NPs for NH_2-NPs and SB-NPs, respectively.

To further confirm the success of the functionalization steps, ζ-potential measurements were conducted (Fig. 2e, Table 1). Pristine NPs displayed negative ζ-potential values typical of deprotonated silanol groups on silica surfaces. Amino-functionalization resulted in a pronounced shift toward positive ζ-potential values for NH_2-NPs, consistent with the high density of surface –NH_2 groups detected by the ninhydrin assay. SB-NPs showed a slight decrease in ζ-potential, reflecting partial shielding or consumption of amino groups. The strong agreement between the ninhydrin and ζ-potential results confirms the stepwise surface modification of the nanoparticles. DLS measurements revealed hydrodynamic diameters significantly larger than those observed by TEM (Table 1), as expected since DLS captures the hydrodynamic radius, including solvation layers and NP aggregates in suspension. These results are consistent with the aggregation observed in TEM images, further validating the characterization.

Overall, the combined TEM, ninhydrin, ζ-potential, and DLS analyses demonstrate that the silica NPs were successfully functionalized with –NH_2 groups and subsequently with SB molecules, and that the nanoparticles remain aggregated in solution. This functionalization is expected to promote the uniform integration of the NPs into polymeric matrices, likely enhancing interfacial compatibility and mechanical strength.

TGA analysis performed in air, as shown in Fig. 2f, reveals no significant weight loss for the pristine SiNPs, consistent with their fully inorganic composition. In contrast, both NH_2-NPs and SB-NPs exhibited distinct mass losses upon heating, confirming the presence of organic functional groups on their surfaces. A major degradation step was detected at 315 °C for NH_2-NPs and at 343 °C for SB-NPs, corresponding to weight losses of 8% w/w and 16% w/w, respectively. The greater mass loss observed for SB-NPs is consistent with their longer organic chains relative to NH_2-NPs.

The surface presence of terminal –NH_2 groups on the NH_2-NPs was confirmed by ATR-FTIR (Fig. 2g), which revealed a characteristic peak at 1560 cm^{-1} absent in unmodified SiNPs. Following the Schiff-base

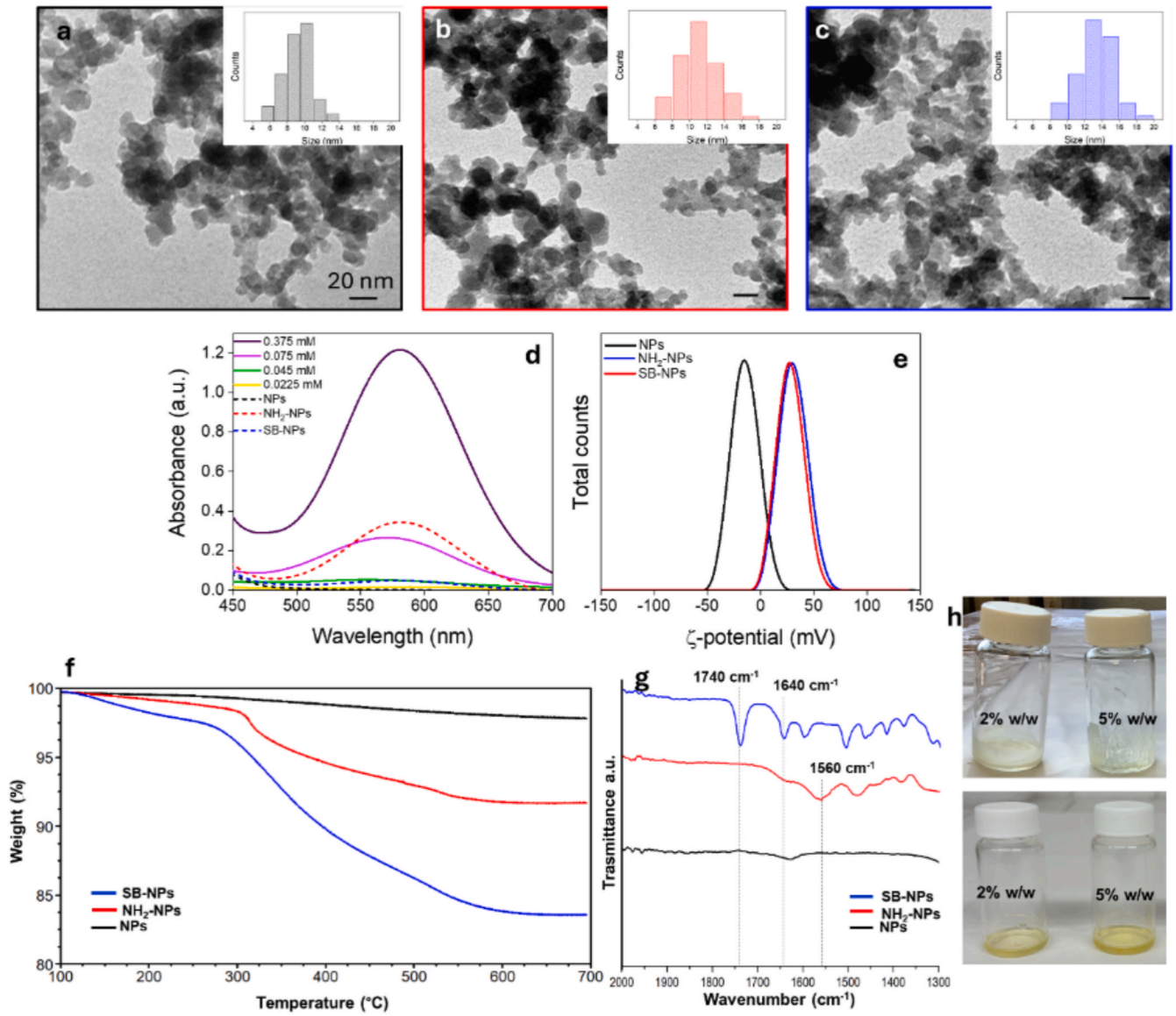

Fig. 2. Characterization of pristine and functionalized silica NPs: TEM images of (a) NPs, (b) NH_2-NPs, and (c) SB-NPs; scale bar: 20 nm. (d) Ninhydrin assay spectra on NPs, NH_2-NPs, and SB-NPs. (e) ζ-potential measurements performed on NPs, NH_2-NPs, and SB-NPs. (f) Thermogravimetric analysis (TGA) of NPs, NH_2-NPs, and SB-NPs. (g) FTIR spectra of NPs, NH_2-NPs, and SB-NPs. (h) Photographs of 2% and 5% w/w NPs (up) and 2% and 5% w/w SB-NPs in the resin (down).

Table 1
Summary of intensity-average hydrodynamic diameter and corresponding PDI determined by DLS and ζ-potential values.

	Size distribution (nm)	PDI	ζ-potential (mV)
NPs	58 ± 3	0.53 ± 0.03	−15.0 ± 1.2
NH_2-NPs	36 ± 4	0.17 ± 0.07	+30.4 ± 0.4
SB-NPs	37 ± 2	0.29 ± 0.01	+28.5 ± 0.6

reaction with MVL, this peak disappears, while a new band emerges at 1640 cm^{-1}, indicative of imine formation, alongside a signal at 1740 cm^{-1} attributable to the ester functionality of MVL. Fig. 2h also highlights how surface functionalization improves NPs dispersion within the resin. Unlike pristine commercial SiNPs, which form a heterogeneous and poorly mixed system, SB-NPs are evenly distributed throughout the resin, resulting in a uniform and stable mixture. This highlights the effectiveness of the Schiff-base modification in promoting homogeneous integration of NPs.

Characterization of free-standing films

To investigate the chemical and physical properties of the resulting networks, free-standing films were prepared according to the procedure described in the Experimental Section. The ATR-FTIR spectra (Fig. 3a) showed that all films shared the same chemical features, with no significant differences between the pristine and composite networks. Though the characteristic signals of ester groups (1710 cm^{-1}) and imine functionalities (1640 cm^{-1}) were detected in all samples [21], a broadening of the imine band was evident in the composites, consistent with the presence of imine linkages both within the polymer network and at the surface of the functionalized nanoparticles. A minor variation was also noted near 1082 cm^{-1} in the 5% w/w SB-NPs sample, attributable to the overlapping of the polymer matrix signal with the asymmetric Si–O–Si stretching of the silica nanoparticles [31,32].

Thermogravimetric analysis (Fig. 3b, **Table S1, Fig. S3**), carried out in air, revealed that the pristine network is thermally stable up to 155 °C, above which three degradation stages occur. The first degradation step exhibits a maximum rate at 237 °C and accounts for a 23% w/w mass

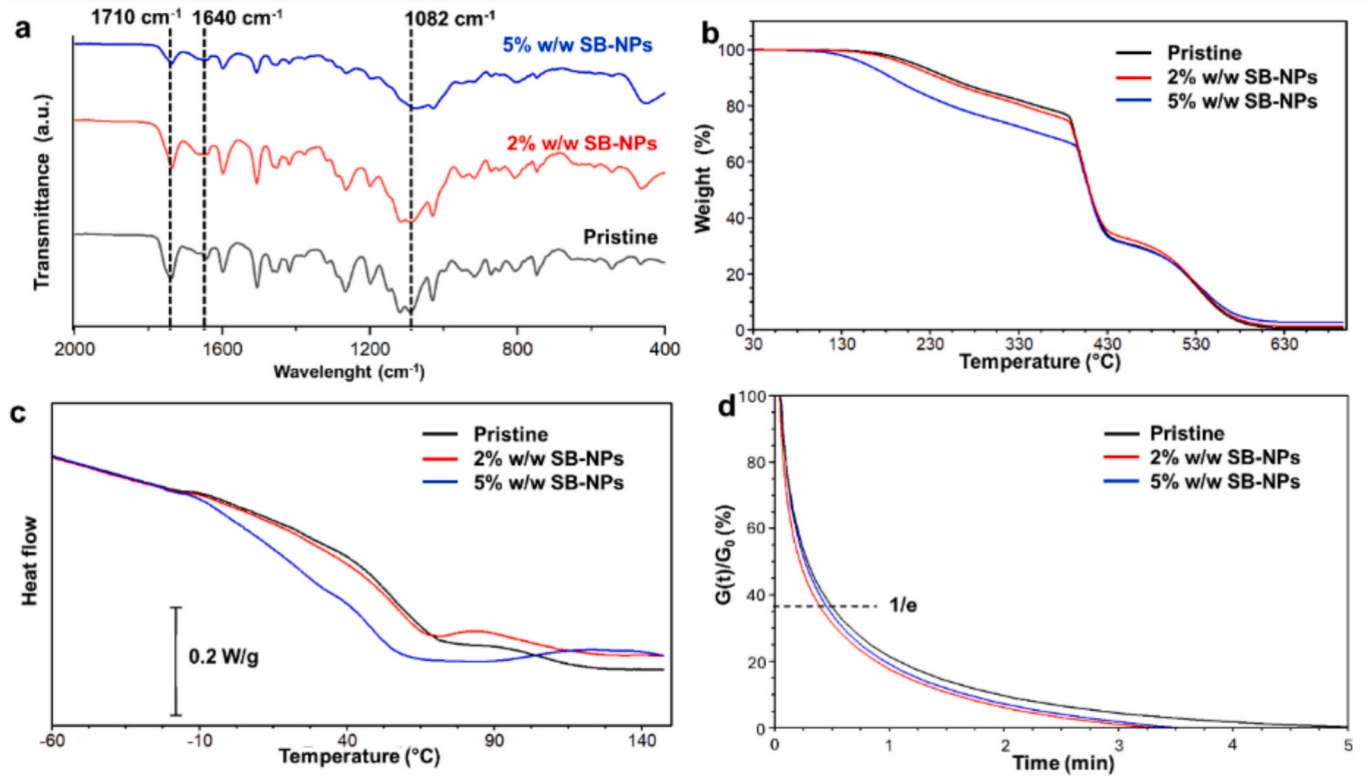

Fig. 3. Characterization of free-standing films. a) ATR-FTIR spectra; b) TGA curves; c) DSC curves; d) stress relaxation analysis performed at 60 °C.

loss. This step can be attributed to the presence of imine functionalities, which generally display lower thermal resistance than permanent covalent bonds. The second step, with a maximum rate at 405 °C, corresponds to an additional 47% w/w mass loss and is ascribed to the random scission of the crosslinked chains [24]. Finally, the last stage, associated with the thermo-oxidation of the carbonaceous residue, shows a maximum rate at 535 °C.

The thermogravimetric profile of the 2% w/w SB-NPs composite closely overlapped that of the pristine sample. In contrast, the 5% w/w SB-NPs composite exhibited reduced thermal stability, with degradation beginning at approximately 100 °C, and a broadened first degradation step, leading to a 34% w/w mass loss. These observations suggest incomplete curing in the 5% w/w formulation [30], a conclusion further supported by additional analyses described below. Under oxidative conditions, no residue remained for the pristine network. However, residual masses of 1.3 and 2.7% w/w were measured for the 2 and 5% w/w SB-NPs samples, respectively. These values correspond to the inorganic fraction of the nanoparticles, as the organic functionalization degraded consistently with the TGA curves in Fig. 2f.

The DSC first heating scans (Fig. 3c, **Table S1**) revealed broad glass transition regions for all formulations, characteristic of crosslinked networks. While the pristine resin and the 2% w/w SB-NPs composite displayed comparable T_g values at around 51 °C, the 5% w/w SB-NPs sample exhibited a lower T_g of 28 °C, again consistent with the presence of uncured material. This trend was corroborated by gel content measurements collected in **Table S1**, which showed high solvent resistance for both the pristine network (89 ± 2% w/w) and the 2% w/w SB-NPs composite (80 ± 6% w/w), but a significantly reduced gel fraction for the 5% w/w sample (70 ± 4% w/w).

Collectively, these results indicate that incorporating SB-NPs at 2% w/w does not substantially alter the physico-chemical properties of the DOM-MVL:MEu vitrimer. However, increasing the nanoparticle loading to 5% w/w, although synthetically feasible, hinders complete network curing, resulting in a material with lower thermal stability, reduced glass transition temperature, and diminished solvent resistance.

The reduced gel content and lower T_g observed for the 5% w/w SB-NPs formulation strongly suggest incomplete network formation. This can be explained by considering the combined optical, physicochemical, and interfacial effects introduced by the higher nanoparticle loading. In UV-curable methacrylate systems, the presence of inorganic nanoparticles influences curing efficiency through multiple mechanisms. First, light scattering and attenuation effects become increasingly relevant at higher filler contents, particularly in the presence of nanoparticle aggregates, as evidenced by SEM and AFM analyses in this study. Even for transparent fillers, such as silica, a mismatch in the refractive index between the inorganic phase and the organic matrix leads to significant scattering of UV radiation. This reduces the effective photon flux that reaches the bulk of the film, thereby decreasing the efficiency with which photoinitiators are activated. This phenomenon has been widely reported in nanoparticle-filled photopolymer systems and is often associated with reduced depth of cure and spatially heterogeneous conversion [33,34].

In addition to optical effects, interfacial interactions between the nanoparticles and reactive species may contribute to the inhibition of curing. SB-functionalized silica nanoparticles retain a residual fraction of surface amino groups, as demonstrated by ninhydrin and ζ-potential analyses. These amines may interfere with the radical photopolymerization process by acting as radical scavengers or by promoting side reactions, such as chain transfer or premature termination [35].

Furthermore, the formation of nanoparticle aggregates at higher loadings introduces significant microstructural heterogeneity, which can locally hinder polymerization. Aggregates can act as physical barriers that limit monomer and radical diffusion, promote early vitrification in confined regions, and ultimately prevent the system from reaching full conversion. This effect is exacerbated by the increase in viscosity associated with higher filler content, which reduces molecular mobility and further restricts the progression of the polymerization reaction [36,37].

Stress relaxation measurements performed at 60 °C are reported in Fig. 3d. The curves illustrate a decrease in the normalized stress

relaxation modulus over time. The stress relaxation modulus decreased by more than 37% in less than 1.5 min for all the samples, with the 2% w/w SB-NPs releasing the stress in the shortest time. This result suggests the occurrence of imine exchange reactions at temperatures slightly above T_g; the presence of SB-NPs further contributes to the activation of the imine associative pathways. However, given that the measurements are performed close to T_g, the contribution from the enhanced chain mobility cannot be excluded.

Characterization of the network as protective coatings

To evaluate the suitability of the synthesized networks as protective coatings, the resins were applied onto glass and steel substrates and subsequently cured. The resulting coatings were characterized in terms of morphology, self-healing behavior, scratch resistance, adhesion to the substrate, and anti-corrosion performance. Finally, we demonstrated the possibility of completely removing the coating from the substrate and recovering its oligomeric species.

The coatings cured on steel substrates were examined by SEM. As expected, the pristine sample exhibits a smooth, and uniform morphology, with no detectable defects or structural irregularities (Fig. 4a). In the case of the 2% w/w SB-NPs formulation, the coating remains generally smooth; however, sub-micrometer sized aggregates are observed, as also highlighted in the inset of Fig. 4b. In contrast, the coating containing 5% w/w SB-NPs displays a markedly heterogeneous surface morphology characterized by the presence of widely distributed aggregates embedded in the polymeric matrix (Fig. 4c) [32,38].

Further insight on the morphological properties of the coatings was obtained via AFM. The pristine sample exhibited two distinct surface types. A representative topography map of the most commonly observed type is shown in Fig. 4d: in agreement with the SEM results, it displays a smooth background (rms roughness $S_q = 3.7$ nm), over which globular aggregates with lateral sizes ranging between ~ 40 and ~ 80 nm can be detected. A representative topography map of the second type of surface (which was observed only in occasional locations) is shown in Fig. 4f: at variance, it displays a corrugated texture ($S_q = 102$ nm) characterized by much larger granular aggregates ranging between ~ 100 and ~ 500 nm in lateral size. Fig. 4e and 4g display the corresponding phase maps,

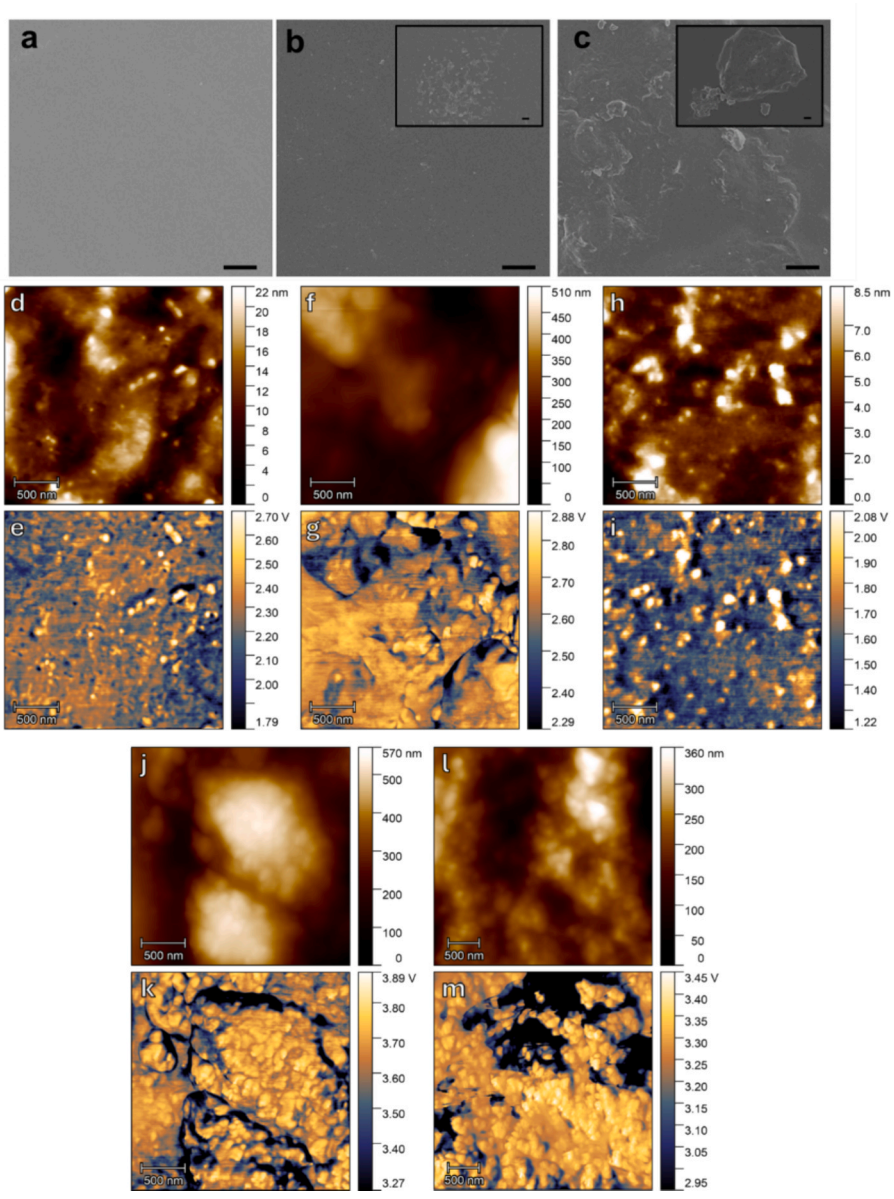

Fig. 4. Scanning electron microscopy of Pristine (a), 2% w/w SB-NPs (b), 5% w/w SB-NPs (c). Atomic force microscopy and corresponding maps of (d-g) pristine, (h-k) 2% w/w SB-NPs, and (l-m) 5% w/w SB-NPs.

which in both cases exhibit a clear contrast throughout the entire image. This contrast suggests a pronounced inhomogeneity in the viscoelasticity and adhesion across the sample surface [39]. This finding can be attributed to the resin curing process that promotes the assembly of differently packed domains [40].

The sample with 2% w/w SB-NPs formulation also displayed two distinct types of surfaces, which were distributed much more evenly throughout the surface – again, in agreement with the SEM results. Fig. 4h and 4i show representative topography and phase maps of the first type of surface, which again display a smooth background ($S_q = 1.6$ nm) and widespread phase contrast. With respect to the flat areas of the pristine sample, however, a much larger number of aggregates with lateral size in the range between ~ 40 and ~ 80 nm can be observed throughout the surface. The topography and phase maps of the second type of surface are shown in Fig. 4j and 4k: these areas exhibit the same long-range structure of the corrugated areas in the pristine sample ($S_q =$ 109 nm and granular aggregates between ~ 100 and ~ 500 nm in lateral size). However, an additional short-range substructure can also be clearly distinguished, composed of smaller grains ranging between ~ 50 and ~ 100 nm in lateral size. This pronounced increase in the short-range granular structure of the sample can be directly attributed to the incorporation of the SiNPs into the resin.

As expected, the prominence of the short-range granular structure increased further in the sample with a 5% w/w SB-NPs formulation, due to the larger incorporation of silica NPs: as a matter of fact, small grains ranging between ~ 50 and ~ 200 nm in lateral size can be clearly distinguished in both the topography (Fig. 4l) and phase (Fig. 4m) maps. Additionally, the overall roughness of the surface decreased in this sample ($S_q = 60$ nm), and large areas of the phase image display an abrupt transition to a featureless contrast (dark blue areas in Fig. 4m). This latter observation suggests that the AFM feedback loop encountered a sudden, stark change in the dissipative tip-sample interaction [39], as may be expected from the tip suddenly scanning over an area of uncured, liquid material. In this context, the reduced surface roughness can be ascribed to a reduced long-range corrugation caused by incomplete sample curing due to the large NPs loading.

The self-healing performance of the coatings was evaluated as a function of the healing temperature on both glass and steel substrates, and the results are documented in Figs. 5 and 6 as well as in Videos **S1-S18**. For each sample and at each healing temperature, images were collected immediately after scratch formation and after 5 min of heating at the selected temperature.

For its chemical nature, the self-healing of the network exploits an intrinsic healing approach. The polymeric network can repair the damage via a temporary increase in mobility, leading to a reflow of the damaged area, followed by a process of restoration of the chemical bonds [1,41]. As documented in **Table S2**, for all coatings and on both substrates (glass and steel), higher healing temperatures lead to shorter scratch-closure times. Since all coatings are in their rubbery state at the tested healing temperatures, the observed trend can be attributed primarily to the enhanced activation of imine exchange reactions at elevated temperatures. In fact, the self-healing kinetics are governed mainly by temperature-dependent imine activation.

Imine exchange has been extensively documented in bulk vitrimers under combined thermal and mechanical stimuli. However, to the best of our knowledge, its appearance in thin coatings has not systematically been investigated yet. The present findings indicate that the low coating thickness, combined with possible interfacial stress at the coating–substrate boundary, is sufficient to promote imine metathesis upon heating, even in the absence of externally applied pressure. In addition, when the healing temperature exceeds T_g, the coating enters a rubbery viscoelastic regime in which surface tension-driven deformation (Laplace pressure at the scratch interface) may contribute to damage closure.

Regarding the performance of individual formulations, the pristine vitrimeric coating exhibited complete scratch reclosure at 120 °C and 100 °C, although a residual furrow remained visible at 100 °C, particularly with glass as the substrate (Fig. 5a). No appreciable healing was observed at 80 °C (Figs. 5a and 6a). Incorporation of SB-NPs at 2% w/w significantly improved healing efficiency, enabling full scratch closure at all tested temperatures (Figs. 5b and 6b). This enhancement can be rationalized by considering that imine exchange may occur not only within the polymer network but also at the polymer-nanoparticle interface. Moreover, because not all amine groups grafted during the APTES functionalization are consumed in the subsequent Schiff-base reaction with MVL, a fraction of free $–NH_2$ groups remains on the SB-

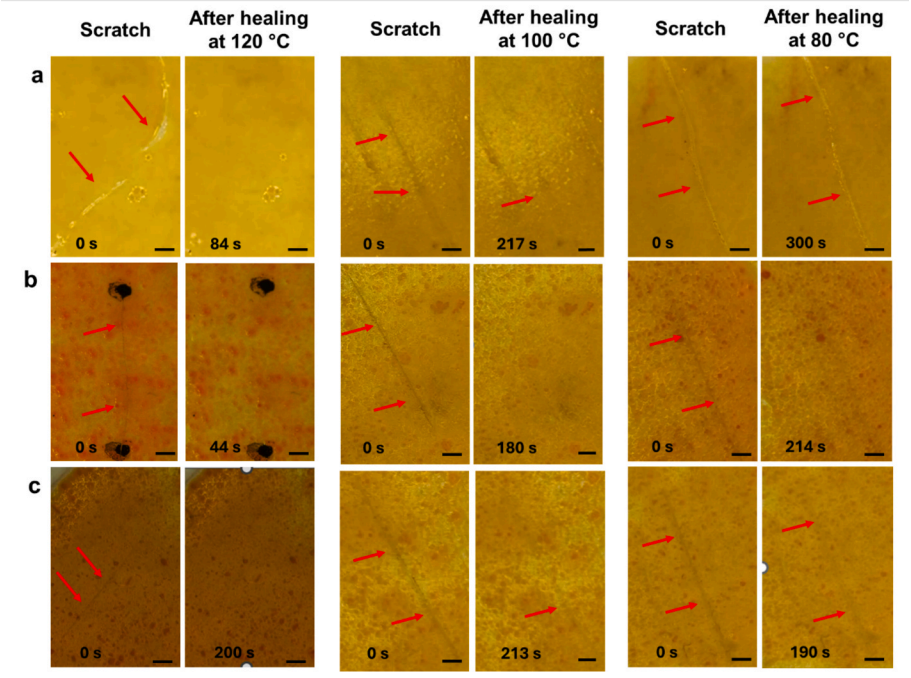

Fig. 5. Snapshots of scratches before and after the healing treatment at 120 °C, 100 °C, and 80 °C on coatings applied on glass. a) Pristine; b) 2% w/w SB-NPs, c) 5% w/w SB-NPs. Scale bar: 1 mm. The corresponding time points at which each snapshot was acquired are indicated in the figure.

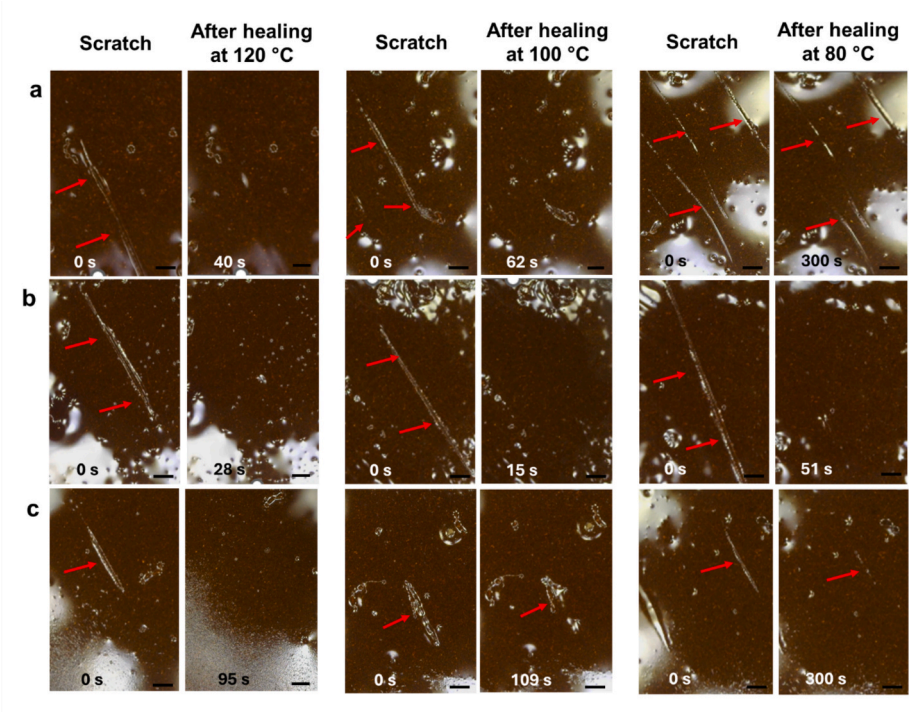

Fig. 6. Snapshots of scratches before and after the healing treatment at 120 °C, 100 °C, and 80 °C on coatings applied on steel. a) Pristine; b) 2% w/w SB-NPs, c) 5% w/w SB-NPs. Scale bar: 1 mm. The corresponding time points at which each snapshot was acquired are indicated in the figure.

NPs surface, as confirmed by ζ-potential measurements. These pendant amines may participate in transimination reactions in addition to imine metathesis, providing an additional dynamic exchange pathway and thereby accelerating the healing process.

In contrast, the coatings containing 5% w/w SB-NPs exhibited poorer healing performance compared to both the pristine and the 2% w/w SB-NPs. Slower or incomplete scratch reclosure was observed at all temperatures (Figs. 5c and 6c). This behavior can be attributed to the morphological inhomogeneity of these coatings, characterized by large nanoparticle aggregates that disrupt network continuity and hinder efficient dynamic bond exchange.

The superior self-healing performance of coatings applied to steel compared to glass can be attributed to steel's higher thermal conductivity, which promotes more uniform and rapid heating of the coating during the test. This was confirmed by localized temperature measurements of the coating surface using a temperature probe, which showed

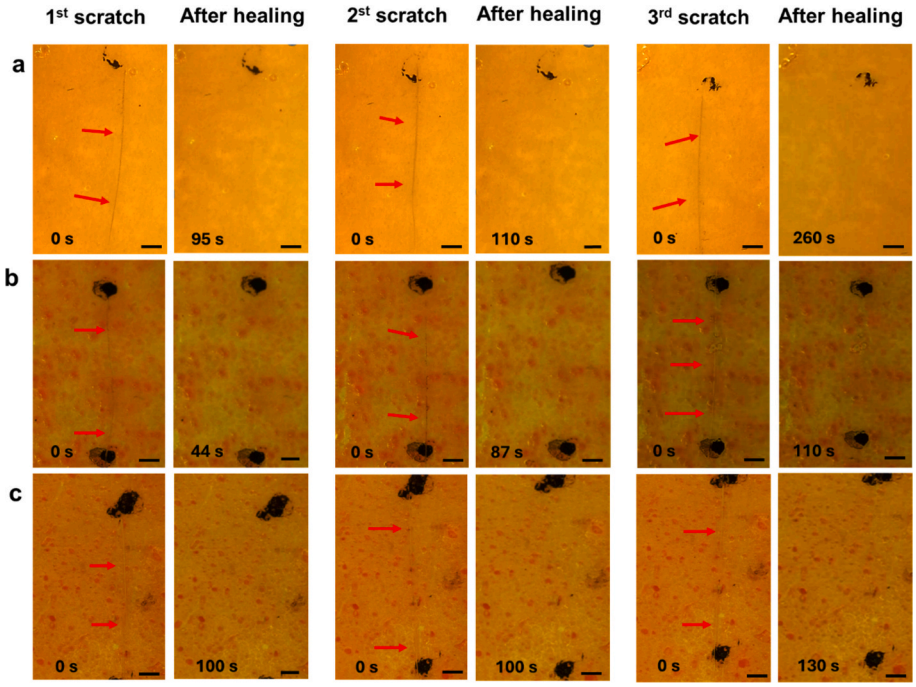

Fig. 7. Multiple self-healing cycles performed at 120 °C on coatings applied on glass. a) Pristine; b) 2% w/w SB-NPs, c) 5% w/w SB-NPs. Scale bar: 1 mm. The corresponding time points at which each snapshot was acquired are indicated in the figure.

that the coating on the steel substrate reached the target temperature approximately 60 s earlier than that on the glass substrate. As a result, the healing process is initiated earlier, leading to an overall acceleration compared to coatings applied on glass.

The coatings applied on glass substrates were also evaluated for their ability to undergo multiple self-healing cycles (Fig. 7, Video **S19-S27**). The healing ability based on an intrinsic mechanism does not require the addition of special healing agents in the polymer matrix. Therefore, the healing mechanism is not restricted to a single occurrence but can be activated and repeated multiple times [6,42].

In the test, three consecutive scratches were introduced sequentially, with each scratch being applied only after the previous one had fully reclosed. Healing was carried out at 120 °C, since this temperature enabled complete reclosure for all formulations. As shown in Fig. 7, full recovery of the scratch was consistently achieved over the three cycles, with the 2% w/w SB-NPs formulation exhibiting the fastest healing response (**Table S3**), in agreement with the results of single-cycle experiments.

A progressive increase in healing time from the first to the third cycle was observed for all samples (**Table S3**). This trend may be attributed to minor chemical or structural changes occurring within the coating during repeated thermal exposure and bond-exchange events, which could slightly reduce the efficiency of the dynamic covalent rearrangements responsible for healing.

Scratch resistance tests, performed in accordance with ASTM D3363–22, were conducted to evaluate the resistance of the coatings to mechanical damage. The results, reported in Fig. 8, show that the incorporation of SB-NPs markedly enhances the scratch resistance of the coatings. While the pristine sample exhibits a well-defined and continuous scratch, neither the 2% w/w nor the 5% w/w SB-NPs formulations display evident scratching when tested with a 6H pencil; conversely, only some graphite marks are visible on the very surface of these coatings.

This improvement can be attributed to two main factors. First, the intrinsic hardness of the SB-NPs is higher than that of the pristine vitrimeric network, thereby increasing the overall resistance of the coating to localized deformation [43]. Second, the chemical compatibility between SB-NPs and the polymer matrix contributes to an effective load transfer during mechanical contact, further enhancing the hardness and scratch resistance of the coating [44,45].

The adhesion strength of the coatings was evaluated using the pull-off test method according to ISO 4624 standard. The schematic of the setup is shown in Fig. 9a. All samples showed sudden failures and brittle behavior. Pristine coating exhibited a mean pull-off strength of 8.7 ± 1.3 MPa, while the addition of 2% w/w NPs yielded a mean value of 8.1 ± 0.5 MPa. Increasing the NPs loading to 5% w/w resulted in a reduction of adhesion strength to 6.6 ± 0.9 MPa (Fig. 9b). Despite the downward trend of the pull-off strength with increasing the NPs loading, statistical analysis performed via one-way ANOVA ($p > 0.05$) indicated that this difference is not statistically significant at 95% confidence level. Consequently, the adhesion of the coating is not influenced by the presence of nanoparticles.

The failure surfaces analysis (Fig. 9**c-d**) revealed the fracture pattern, identifying the components responsible for the loss of adhesion. Notably, no adhesive failure between the coating and the metal substrate (CS) was observed for any formulation (CS = 0%), demonstrating that the interfacial compatibility between the coating and the steel substrate is robust. All tests revealed that the failures involved the system made by the cyanoacrylate glue and the coating. In particular, a prevalent adhesive failure at the interface between the glue and the coating was observed, rather than cohesive failure of the coating itself. The pristine samples exhibited a mixed failure mode (30% CC, 70% GC); the separation occurred primarily at the adhesive-coating interface, while approximately one-third of the area was characterized by cohesive failure within the coating layer. In the case of 2% w/w SB-NPs, the cohesive failure fraction (CC) decreased to 20%, as the failure shifted

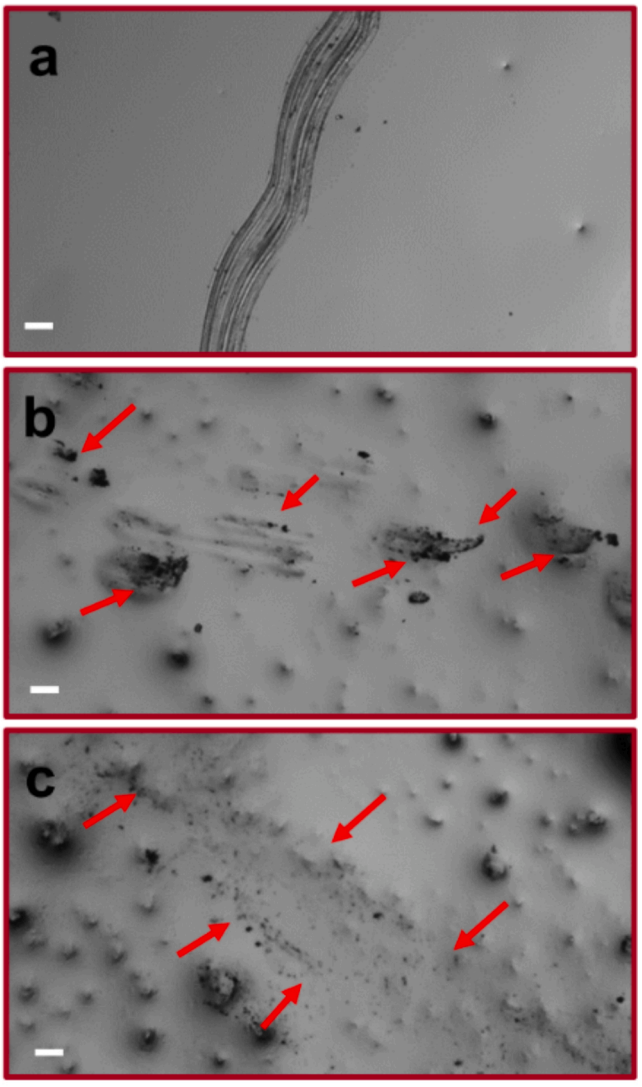

Fig. 8. Scratch test performed according to ASTM D3363–22 on a) pristine, b) 2%w/w SB-NPs, c) 5% w/w SB-NPs.

predominantly to the glue-coating interface (GC, 80%). Conversely, the 5% w/w SB-NPs formulation reverted to a failure pattern comparable to the pristine one (30% CC, 70% GC). Accordingly, the measured pull-off strength values should be regarded as a lower bound of the actual coating-substrate adhesion, as failure is governed by the glue-coating interface or by cohesive rupture within the coating rather than by interfacial detachment from the steel substrate.

The barrier properties and the corrosion protection effectiveness of the coatings were assessed using EIS measurements during immersion in a saline solution. The results are reported in Fig. 10 as Bode diagrams. As can be seen from the impedance modulus, the formulations exhibit different behaviors (please note that the y-axis scale is different for the 5% w/w SB-NPs sample). Indeed, the pristine sample is characterized by a high impedance modulus at the beginning of the test ($|Z|$ measured at 0.01 Hz close to 10^9 Ω·cm^2 after 1 h of immersion in the electrolyte) and a capacitive behavior, with phase values close to −90° for a large portion of the spectrum. After only 24 h of immersion, a significant decrease in impedance modulus is observed, dropping to $2{\cdot}10^7$ Ω·cm^2. This value then stabilizes at approximately 10^7 Ω·cm^2 over the following days. Such behavior is characteristic of organic coatings containing polar functional groups, such as imine and ester moieties present in the network, and can be associated with water uptake within the polymer

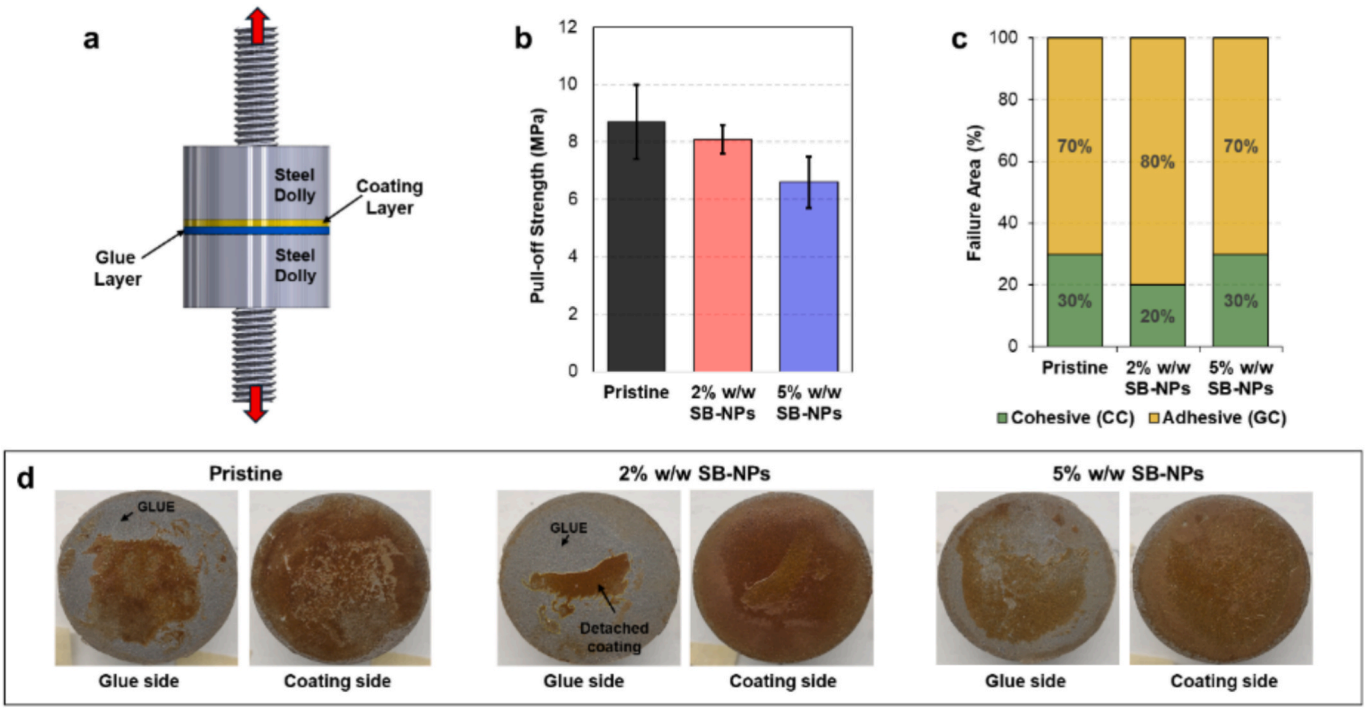

Fig. 9. Adhesion properties of the coatings evaluated via pull-off test according to the ISO 4624 standard. (a) Schematic of the setup. (b) Mean pull-off strength values; error bars represent the standard deviation; measurements were performed in triplicate (c) Quantitative distribution of failure modes (CC: Cohesive Failure within the coating; GC: Adhesive Failure at the glue/coating interface). Percentage areas are rounded to the nearest 10% in accordance with ISO 4624 recommendations. (d) Representative optical images of the fracture surfaces (glue side and coating side), showing the reduced cohesive failure area in the 2% w/w formulation compared to the Pristine and 5% w/w samples.

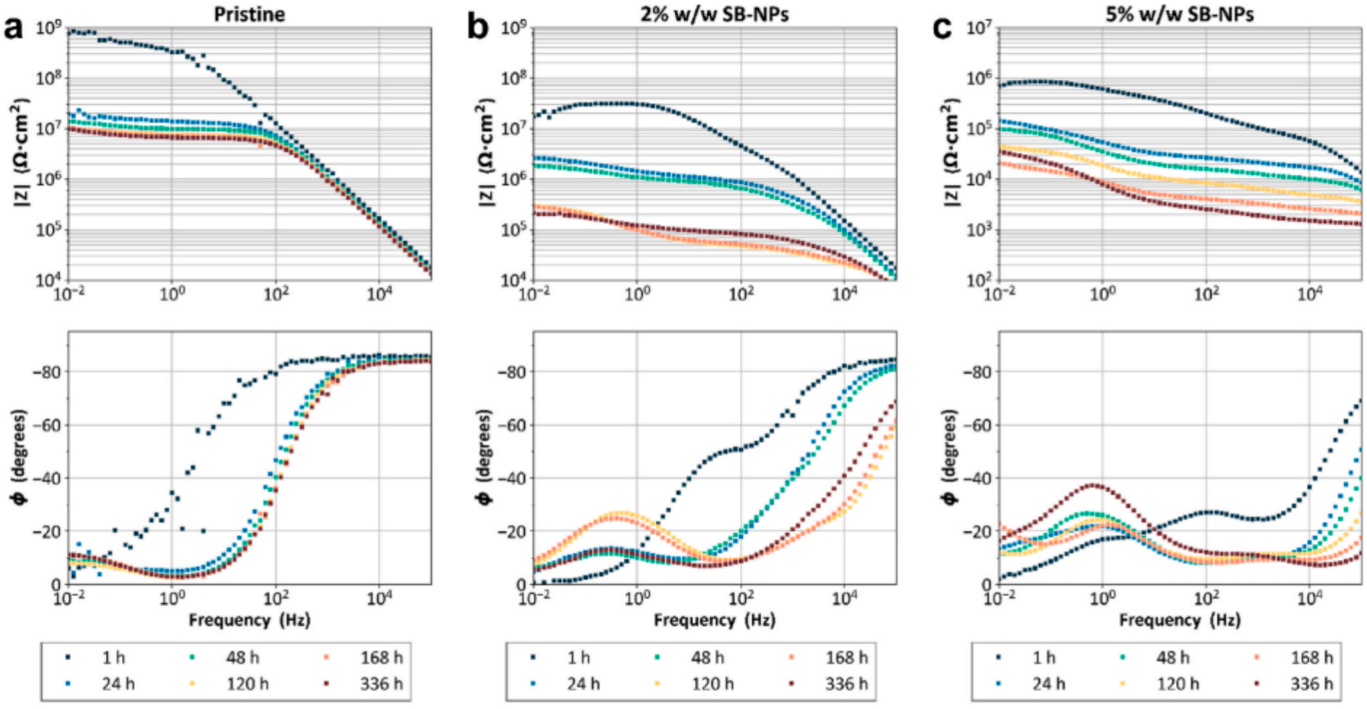

Fig. 10. EIS spectra acquired on the Pristine (a), 2% w/w SB-NPs (b), and 5% w/w SB-NPs (c) during immersion for 336 h in 3.5% w/w NaCl solution. For clarity, the y-axis uses a different scale in the plot displaying the spectra of the 5% w/w SB-NPs sample.

matrix [46]. Indeed, such a phenomenon causes the modification of the coating capacitance (due to the different dielectric constant of the water and of the resin) and significantly decreases the coating resistance, due to the diffusion of water molecules and ions inside the polymer network. This process is further highlighted by the appearance of a second time constant (already visible after 24 h of immersion) in the low-frequency part of the spectrum, identifiable as the small peak in the phase close to 0.01 Hz [47]. Despite the decrease in impedance, it can be concluded

that the coatings provide sufficient protection for the steel substrate throughout the immersion test. Indeed, it is generally recognized that the organic coating provides corrosion protection if the impedance modulus measured at 0.01 Hz exceeds 10^5 Ω·cm^2 [48,49].

The 2% w/w SB-NPs samples exhibit a different behavior, as they are characterized by a lower impedance modulus from the beginning of the test (|Z| measured at 0.01 Hz close to $2{\cdot}10^7$ Ω·cm^2 after 1 h of immersion in the electrolyte), which further decreases during immersion, reaching about $2{\cdot}10^5$ Ω·cm^2 after 168 h. The weaker corrosion protection is further highlighted by the trend of the impedance phase, which is closer to resistive-like behavior than to capacitive-like behavior. Also in this case, the uptake of water inside the polymer is indicated by the appearance of a second time constant in the low-frequency part of the spectrum (peak centered close to 1 Hz).

The decrease in the anti-corrosion efficiency caused by the filler addition may be justified by the shape of the silica particles. In fact, the spherical geometry is less effective in hindering the diffusion of water and ions from the electrolyte toward the metal surface. As already shown in other studies [50–52], a more substantial improvement in the barrier properties can be achieved using lamellar fillers, which can significantly increase the tortuosity of the diffusion path [53] and thus guarantee a better corrosion protection effectiveness.

The least protective behavior was found for the 5% w/w SB-NPs samples, which exhibit a low impedance modulus and phase. The impedance modulus measured at low frequency rapidly decreases from about 10^6 Ω·cm^2 to 10^5 Ω·cm^2 and below, demonstrating a poor corrosion protection effectiveness. Moreover, the impedance phase remains above −40° for a very large portion of the spectrum, indicating a resistive-like behavior and further confirming the indications from the measured modulus values. This poor performance can be associated with the other analyses performed on this formulation. Indeed, as discussed before, 5% w/w SB-NPs samples are characterized by incomplete curing, which leads to a lower glass transition temperature and a lower solvent resistance. The higher mobility of the polymeric network is detrimental to the barrier properties, as it does not sufficiently hinder the diffusion of water and ions from the electrolyte to the metal surface and thus is not effective for corrosion protection.

As shown in the previous section of the study, the developed coatings exhibit interesting self-healing properties upon heating. For this reason, an additional test was performed to assess whether the healing process can effectively restore barrier properties. To this aim, the impedance spectrum was acquired on an intact coating, then after making a 1-cm scratch using a blade and finally after heating the sample for 2 min at 120 °C. This investigation was performed on pristine samples, as they demonstrated the best corrosion protection effectiveness in the previous test. The results are presented in Fig. 11 as a Bode diagram. As can be seen, the presence of the defect sharply reduces the impedance modulus, which goes from about 10^{10} Ω·cm^2 (intact coating, 'initial' in the plot) to about 10^7 Ω·cm^2 in the presence of the cut ('scratch' in the plot). The healing process leads to a new increase in the impedance modulus, which reaches 10^8 Ω·cm^2. Even though a full recovery of the barrier properties is not observed, the achievement is still satisfactory because an adequate protection effectiveness is restored in the coating. Moreover, such a result aligns with similar tests performed on dynamic reversible imine-based coatings [17], in which it was demonstrated that the healing process recovers the barrier properties of the material only partially.

The same test was carried out on the 5% w/w SB-NPs sample and the results are shown in Fig. S4. In this case, healing was performed by heating the coating at 100 °C for 2 min. This condition was selected because, based on the healing test, it should not lead to complete scratch closure. As expected, the impedance modulus decreases due to the presence of the scratch and does not recover after heating. This indicates that full functional recovery is not achieved, likely due to defects that permit electrolyte diffusion into the coating, thereby compromising its barrier properties.

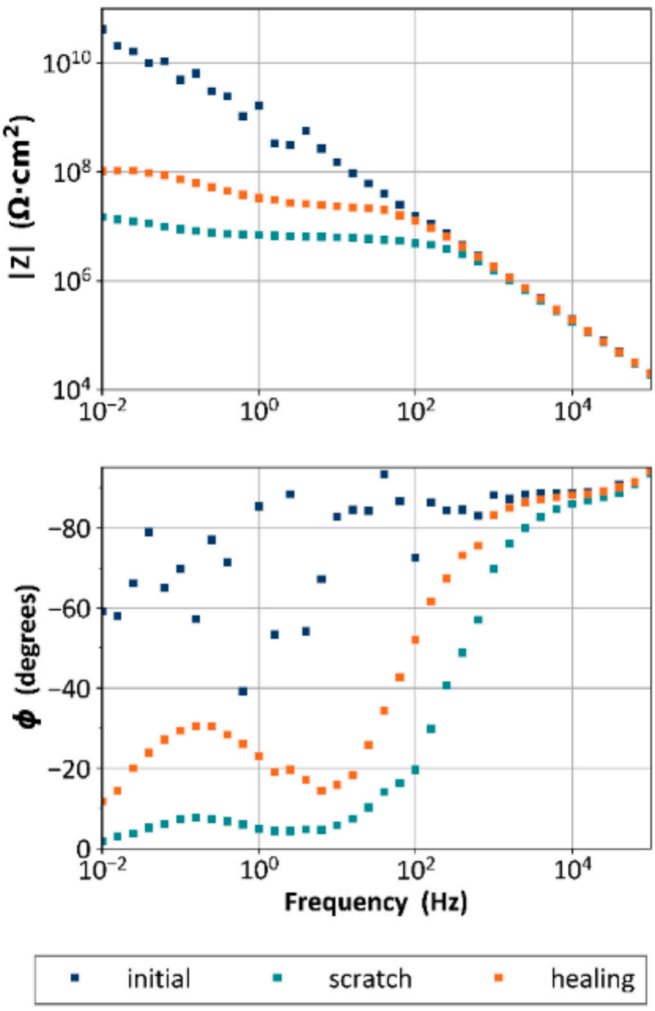

Fig. 11. EIS spectra acquired on pristine sample after immersion in the saline solution ('initial'), after the realization of the 1-cm cut ('scratch'), and after the healing process ('healing').

Decomposition of the coating and recovery of polymeric components

The ability to decompose the coating and to remove it from the substrate was evaluated for both the pristine and the 5% w/w SB-NPs networks applied to glass substrates. As shown in Video**s S28-S29** and schematically reported in Fig. 12a, immersion in an excess of ethylenediamine triggered transimination reactions between the imine bonds within the coating and the primary amines of ethylene diamine, ultimately leading to network depolymerization [21,54]. Following this process, which is different from those previously reported in literature based on the dissociation of imine bonds [43], the glass substrates were fully stripped and appeared perfectly clean. The oligomeric fragments generated during depolymerization were recovered by precipitation in water and subsequent filtration.

The complete elimination of the coating was confirmed by ATR-FTIR spectra (Fig. 12d and 12e) collected on bare glass and on the glass substrate after coating removal: no characteristic peaks of the polymer were detected after treatment, while the silica band at 900 cm^{-1} was clearly visible. Conversely, the recovered oligomeric fragments exhibited a chemical structure closely resembling that of the original coating, as demonstrated by the presence of the imine stretching band at 1640 cm^{-1} in both the coatings and the depolymerized products. The free-standing films obtained by mixing the oligomeric fragments with MV followed by hot pressing showed a compact and homogeneous morphology, as shown in Fig. 12b and 12c. Their chemical structure, as

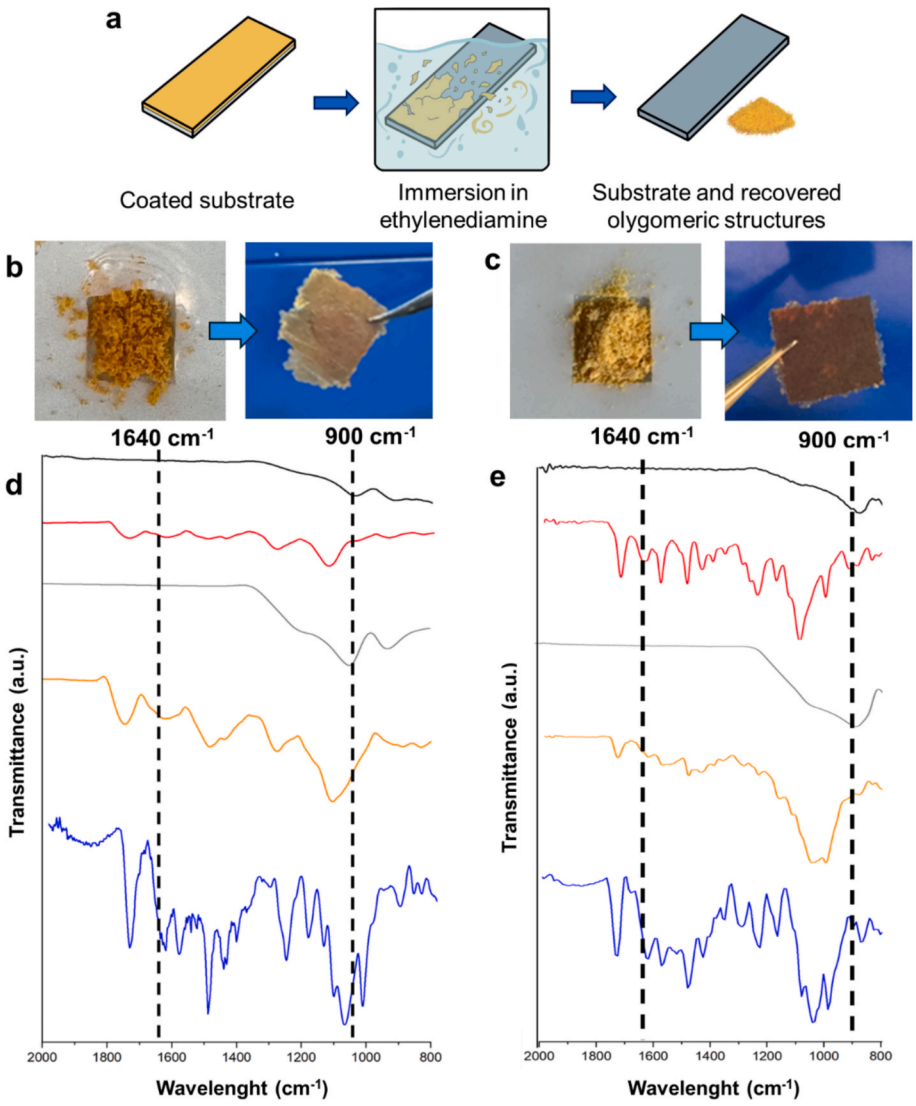

Fig. 12. Deconstruction of the coatings, removal from the substrate, and reuse of the resulting oligomeric fragments to obtain chemically recycled free-standing films. (a) Schematic representation of the degradation and delamination process. Photographs of the recovered oligomeric fragments from pristine samples (b) and 5% w/w SB-NPs samples (c), along with the corresponding free-standing films obtained after mixing with MV followed by hot pressing. (d) ATR-FTIR spectra of bare glass (black), glass coated with the pristine sample (red), glass after coating removal (gray), recovered oligomeric fragments (orange), and chemically recycled free-standing film (blue). (c) ATR-FTIR spectra of bare glass (black), glass coated with the 5% w/w SB-NPs (red), glass after coating removal (gray), the recovered oligomeric fragments (orange), and chemically recycled free-standing film (blue). (For interpretation of the references to colour in this figure legend, the reader is referred to the web version of this article.)

confirmed by ATR-FTIR spectra (Fig. 12d and 12e), is similar to that of the original coating, with a clearly visible imine stretching band.

TGA analysis (**Fig. S5**) revealed that the chemically recycled samples exhibit a thermal degradation behavior largely comparable to that of the corresponding virgin materials, indicating that the recycling process preserves the main thermal features of the system. However, slight differences can be observed. In the pristine system, the recycled sample shows a marginally lower thermal stability at intermediate temperatures, whereas at higher temperatures the degradation profiles tend to converge. A similar trend is observed for the 5% w/w SB-NPs system, where the recycled material displays a slightly more gradual weight loss in the main decomposition region. Overall, these results suggest that the recycling procedure only mildly affects the thermal stability, without significantly altering the degradation mechanism.

Conclusions

In this work, a solvent-free, bio-based vitrimeric system platform based on dynamic imine chemistry has been developed as a multifunctional solution for surface protection. The UV-curable covalent adaptable networks exhibit intrinsic self-healing behavior activated by moderate heating, efficient stress relaxation, and enable complete coating removal and substrate regeneration. The functionalization of silica nanoparticles allows their covalent integration into the network, ensuring homogeneous dispersion and effective interfacial compatibility. At low filler content (2% w/w), the functionalized nanoparticles accelerate scratch reclosure, enabling complete healing at reduced temperatures and markedly improving scratch resistance. Pull-off tests confirm robust coating-substrate interfacial integrity for all formulations, with only a marginal dependence of adhesion strength on nanoparticle loading. Electrochemical impedance spectroscopy measurements demonstrate that the vitrimeric coatings provide effective long-term corrosion protection in saline environments, while the presence of silica nanoparticles increases water uptake, hence limiting barrier performance at higher loadings. Considering the corrosion protection effectiveness, the best performance was achieved by the pristine

samples, which preserved satisfactory barrier properties even after 336 h of immersion in the saline solution. Overall, this study highlights the delicate balance between dynamic network chemistry, filler functionalization, and coating architecture in governing the macroscopic performance of self-healing protective systems.

Data availability

The raw experimental data supporting the findings of this study are available in the [AMS Acta] repository. The dataset can be accessed at https://amsacta.unibo.it/id/eprint/8895/ (DOI https://doi.org/10.6092/unibo/amsacta/8895).

Declaration of competing interest

The authors declare that they have no known competing financial interests or personal relationships that could have appeared to influence the work reported in this paper.

Acknowledgments

Luigi Gamberini acknowledges the European Union -NextGenerationEU (National Sustainable Mobility Center CN00000023, Italian Ministry of University and Research Decree n.1033 - 17/06/2022, Spoke 11 - Innovative Materials & Lightweighting).

Appendix A. Supplementary data

Supplementary data to this article can be found online at https://doi.org/10.1016/j.jiec.2026.04.045

References

[1] S.J. García, H.R. Fischer, S. van der Zwaag, A critical appraisal of the potential of self-healing polymeric coatings, Prog. Org. Coat. 72 (2011) 211–221, https://doi.org/10.1016/j.porgcoat.2011.06.016.
[2] R.D. Maalihan, M.R.B. Domalanta, A.C.C. Corrales, E.B. Caldona, Advances in interfacially engineered surface-functionalized fillers for multifunctional polymer composite coatings, Polym. Comp. 46 (2025) 5857–5881, https://doi.org/10.1002/pc.29358.
[3] R. Teijido, L. Ruiz-Rubio, A. Gallardo Echaide, J.L. Vilas-Vilela, S. Lanceros-Mendez, Q. Zhang, State of the art and current trends on layered inorganic-polymer nanocomposite coatings for anticorrosion and multi-functional applications, Prog. Org. Coat. 163 (2022) 106684, https://doi.org/10.1016/j.porgcoat.2021.106684.
[4] R.A.T.M. van Benthem, W. Ming, G. de With, 2007. Self Healing Polymer Coatings. In: van der Zwaag, S. (eds) Self Healing Materials. Springer Series in Materials Science, vol 100. Springer, Dordrecht. 10.1007/978-1-4020-6250-6_7.
[5] S.M. Chhipa, S. Sharma, A.K. Bagha, Recent development in polymer coating to prevent corrosion in metals: a review, Mater. Today Proc. (2024), https://doi.org/10.1016/j.matpr.2024.09.001.
[6] I.L. Hia, V. Vahedi, P. Pasbakhsh, Self-Healing Polymer Composites: prospects, challenges, and applications, Polym. Rev. 56 (2016) 225–261, https://doi.org/10.1080/15583724.2015.1106555.
[7] J. Sokjorhor, T. Yimyai, R. Thiramanas, D.J. Crespy, Self-healing, antibiofouling and anticorrosion properties enabled by designing polymers with dynamic covalent bonds and responsive linkages, J. Mater. Chem. B 12 (2024) 6827–6839, https://doi.org/10.1039/D4TB00736K.
[8] B. Li, P.F. Cao, T. Saito, A.P. Sokolov, Intrinsically Self-Healing Polymers: from Mechanistic Insight to current challenges, Chem. Rev. 123 (2023) 701–735, https://doi.org/10.1021/acs.chemrev.2c00575.
[9] K. Liang, X. Qi, X. Xiao, L. Wang, J. Zhang, Tannic Acid-based Hyperbranched polyurethane with Superior Mechanical Properties, Room-Temperature Self-Healability, and Ultrahigh Adhesion for Scalable Production, Macromol 58 (2025) 11216–11228, https://doi.org/10.1021/acs.macromol.5c02072.
[10] K. Liang, C. Wang, H. Fan, W. Du, M. Zhang, G. Li, Z. Li, J. Tang, J. Zhang, D. Xue, L. Wang, Fast room-temperature and water-insensitive self-healing polyurethane for superior composite anti-corrosion coating on Mg alloys, Prog. Org. Coat. 198 (2025) 108876. https://www.sciencedirect.com/science/article/pii/S0300944024006684.
[11] K. Liang, X. Qi, Xu. Xiao, J. Li Wang, Zhang,, Chemically-informed active learning enables data-efficient multi-objective optimization of self-healing polyurethanes, Chem. Sci. 17 (2026) 3627–3638. https://pubs.rsc.org/en/content/articlelanding/2026/sc/d5sc07752d.
[12] X. Chen, M.A. Dam, K. Ono, A. Mal, H. Shen, S.R. Nutt, K. Sheran, F.A. Wudl, Thermally Re-mendable Cross-Linked Polymeric Material, Science 295 (2002) 1698–1702, https://doi.org/10.1126/science.1065879.
[13] N. Zheng, Y. Xu, Q. Zhao, T. Xie, T., Dynamic Covalent Polymer Networks: a Molecular Platform for Designing Functions beyond Chemical Recycling and Self-Healing, Chem. Rev. 121 (2021) 1716–1745, https://doi.org/10.1021/acs.chemrev.0c00938.
[14] Y.X. Lu, Z. Gyan, Olefin Metathesis for Effective Polymer Healing via Dynamic Exchange of strong Carbon–Carbon double bonds, J. Am. Chem. Soc. 134 (2012) 14226–14231, https://doi.org/10.1021/ja306287s.
[15] Z.P. Zhang, M.Z. Rong, M.Q. Zhang, C. Yuan, Alkoxyamine with Reduced Homolysis Temperature and its Application in Repeated Autonomous, Polym. Chem. 4 (2013) 4648–4654, https://doi.org/10.1039/C3PY00679D.
[16] F. Van Lijsebetten, S. Engelen, E. Bauters, W. Van Vooren, M.M.J. Smulders, F. E. Du Prez, Recyclable vitrimer epoxy coatings for durable protection, Eur. Polym. J. 176 (2022) 111426, https://doi.org/10.1016/j.eurpolymj.2022.111426.
[17] Y. Li, F. Chang, G. Wei, L. Ren, C. Ji, B. Zhu, C. Xu, Sub-zero temperature self-healing anticorrosion coatings based on dynamic reversible imine and metal coordination bonds, Prog. Org. Coat. 209 (2025) 109629, https://doi.org/10.1016/j.porgcoat.2025.109629.
[18] F. Wang, X. Lu, Z. Xin, Self-healing biobased polybenzoxazine vitrimers for anticorrosion application, Prog. Org. Coat. 203 (2025) 109168, https://doi.org/10.1016/j.porgcoat.2025.109168.
[19] S. Yang, H. Hu, Z. Tong, H. Lin, H. Zeng, Y. Hu, Z. Yang, Vanillin-based imine curing agent for high-strength, recyclable, aging-resistant, and anticorrosive epoxy composite coatings, Compos. Sci. Technol. 270 (2025) 111282, https://doi.org/10.1016/j.compscitech.2025.111282.
[20] H. Shahali, M.A. Rahman, C. Suarez, A. Raut, A.A. Polycarpou, A. Amiri, Infrared-Assisted healing and corrosion protection of aromatic thermosetting copolyester vitrimer coatings in various pH environments, ACS Appl. Polym. Mat. 7 (2025) 6739–6751, https://doi.org/10.1021/acsapm.5c00306.
[21] A. Liguori, S. Subramaniyan, J.G. Yao, M. Hakkarainen, Photocurable extended vanillin-based resin for mechanically and chemically recyclable, self-healable and digital light processing 3D printable thermosets, Eur. Polym. J. 178 (2022) 111489, https://doi.org/10.1016/j.eurpolymj.2022.111489.
[22] Y. Xu, K. Odelius, M. Hakkarainen, Photocurable, Thermally Reprocessable, and Chemically Recyclable Vanillin-based Imine Thermosets, ACS Sustain. Chem. Eng. 8 (2020) 17272–17279, https://doi.org/10.1021/acssuschemeng.0c06248.
[23] A. Liguori, H. Xu, M. Hakkarainen, Simple Non-Equilibrium Atmospheric Plasma Post-Treatment Strategy for Surface Coating of Digital Light Processed 3D-printed Vanillin-based Schiff-Base Thermosets, ACS Appl. Polym. Mater. 5 (2023) 8506–8517, https://doi.org/10.1021/acsapm.3c01632.
[24] A. Liguori, N.K. Kalita, G. Adamus, M. Kowalczuk, M.L. Focarete, M. Hakkarainen, Bio-based ester- and ester-imine resins for digital light processing 3D printing: the role of the chemical structure on reprocessability and susceptibility to biodegradation under simulated industrial composting conditions, Eur. Polym. J. 219 (2024) 113384, https://doi.org/10.1016/j.eurpolymj.2024.113384.
[25] E. Fanizza, H. Zhao, S. De Zio, N. Depalo, F. Rosei, A. Vomiero, M.L. Curri, M. Striccoli, Encapsulation of dual Emitting Giant Quantum Dots in Silica Nanoparticles for Optical Ratiometric Temperature Nanosensors, Appl. Sci. 10 (2020) 2767, https://doi.org/10.3390/app10082767.
[26] T. Latronico, F. Rizzi, A. Panniello, V. Laquintana, I. Arduino, N. Denora, E. Fanizza, S. Milella, C.M. Mastroianni, M. Striccoli, M.L. Curri, G.M. Liuzzi, N. Depalo, Luminescent PLGA Nanoparticles for delivery of Darunavir to the Brain and Inhibition of Matrix Metalloproteinase-9, a Relevant Therapeutic Target of HIV-Associated Neurological Disorders, ACS Chem. Neurisci. 12 (2021) 4286–4301, https://doi.org/10.1021/acschemneuro.1c00436.
[27] D. Nečas, P. Klapetek, Gwyddion: an open-source software for SPM data analysis, Open Phys. 10 (2011) 181–188, https://doi.org/10.2478/s11534-011-0096-2.
[28] Paints and varnishes — Pull-off test for adhesion, ISO 4624:2023, International Organization for Standardization, Geneva, Switzerland, 2023.
[29] J. Schindelin, I. Arganda-Carreras, I., E. Frise,, et al., Fiji: an open-source platform for biological-image analysis, Nat. Methods 9 (2012) 676–682, https://doi.org/10.1038/nmeth.2019.
[30] A. Liguori, E. Oliva, M. Sangermano, M. Hakkarainen, Digital Light Processing 3D Printing of Isosorbide- and Vanillin-based Ester and Ester–Imine Thermosets: Structure–Property Recyclability Relationships, ACS Sustain. Chem. Eng. 11 (2023) 14601–14613, https://doi.org/10.1021/acssuschemeng.3c04362.
[31] M. Mohammadi, M.K. Khorrami, H. Vatanparast, H. Ghasemzadeh, Prediction of surface tension of solution in the presence of hydrophilic silica nanoparticle and anionic surfactant by ATR-FTIR spectroscopy and chemometric methods, Spectrochim. Acta A Mol. Biomol. Spectrosc. 255 (2021) 119697, https://doi.org/10.1016/j.saa.2021.119697.
[32] L.S. Karimi, S. Amiri, M.H. Zori, Synthesis and Characterization of Anti-Scratch and Anti-Corrosion Hybrid Nanocomposite Coatings based on Sol-Gel Process, SILICON 13 (2021) 2195–2207, https://doi.org/10.1007/s12633-020-00721-w.
[33] M. Sadej, E. Andrzejewska, B. Kurc, H. Gojzewski, T. Jesionowski, Surface-dependent effect of functional silica fillers on photocuring kinetics of hydrogel materials, J. Polym. Sci. A Polym. Chem. 52 (2014) 3472–3487, https://doi.org/10.1002/pola.27412.
[34] Z. Yang, J. Wu, G. Ma, C. Hou, Y. Niu, H. Duan, X. Hao, Effect of the particle sizes of silica on the properties of UV-curing matting coatings, J. Coat. Technol. Res. 18 (2021) 183–192, https://doi.org/10.1007/s11998-020-00395-4.
[35] M. Jankowska, O. Ozukanar, E. Çakmakçi, J. Ortyl, A thiol-functional amine synergist as a co-initiator for DLP 3D printing applications, Polym. Chem. 16 (2025) 3895–3915, https://doi.org/10.1039/d5py00603a.
[36] M.R. Azani, A. Hassanpour, UV-Curable Polymer Nanocomposites: Material selection, Formulations, and recent advances, J. Compos. Sci. 8 (2024) 441, https://doi.org/10.3390/jcs8110441.

[37] P. Hu, H. Xu, Y. Pan, Z. Sang, R. Liu, Upconversion particle-assisted NIR polymerization enables microdomain gradient photopolymerization at inter-particulate length scale, Nat. Commun. 14 (2023), https://doi.org/10.1038/s41467-023-39440-2.
[38] Z.X. Li, Y.S. Xiang, Y. Ran, Well-dispersed silica nanoparticle-reinforced epoxy vitrimer composites prepared by dynamic crosslinking, J. Mater. Sci. 58 (2023) 17470–17482, https://doi.org/10.1007/s10853-023-09126-7.
[39] R. García, J. Tamayo, M. Calleja, et al., Phase contrast in tapping-mode scanning force microscopy, Appl. Phys. A 66 (1998) S309–S312, https://doi.org/10.1007/s003390051152.
[40] M. Sadej, E. Andrzejewska, B. Kurc, H. Gojzewski, T. Jesionowski, Surface-dependent effect of functional silica fillers on photocuring kinetics of hydrogel materials, J. Polym. Sci. A Polym. Chem. 52 (2014) 3472–3487, https://doi.org/10.1002/pola.27412.
[41] B. Li, P.F. Cao, T. Saito, A.P. Sokolov, Intrinsically Self-Healing Polymers: from Mechanistic Insight to current challenges, Chem. Rev. 123 (2023) 701–735, https://doi.org/10.1021/acs.chemrev.2c00575.
[42] S.H. Pezzin, Mechanism of Extrinsic and Intrinsic Self-healing in Polymer Systems, in: N. Hameed, J.C. Capricho, N. Salim, S. Thomas (Eds.), Multifunctional Epoxy Resins, Engineering Materials, Springer, Singapore, 2023.
[43] J. Liu, K.V. Bernaerts, Preparation of lignin-based imine vitrimers and their potential application as repairable, self-cleaning, removable and degradable coatings, J. Mater. Chem. A 12 (2024) 2959–2973, https://doi.org/10.1039/D3TA06338K.
[44] D. Morselli, F. Bondioli, M. Sangermano, M. Messori, Photocured epoxy networks reinforced with TiO2 in-situ generated by means of non-hydrolytic sol-gel process, Polymer 5 (2012) 283–290, https://doi.org/10.1016/j.polymer.2011.12.006.
[45] X.F. Yang, D.E. Tallman, V.J. Gelling, G.P. Bierwagen, L.S. Kasten, J. Berg, Use of a sol–gel conversion coating for aluminum corrosion protection, Surf. Coat. Technol. 140 (2001) 44–50, https://doi.org/10.1016/S0257-8972(01)01002-7.
[46] R.G. Duarte, A.S. Castela, M.G.S. Ferreira, A new model for estimation of water uptake of an organic coating by EIS: the tortuosity pore model, Prog. Org. Coat. 65 (2009) 197–205, https://doi.org/10.1016/j.porgcoat.2008.11.007.
[47] M. Dornbusch, S. Kirsch, C. Henzel, C. Deschamps, S. Overmeyer, K. Cox, M. Wiedow, U. Tromsdorf, M. Dargatz, U, Meisenburg, Characterization of the water uptake and electrolyte uptake of organic coatings and the consequences by means of electrochemical impedance spectroscopy and UV–vis spectroscopy, Prog. Org. Coat. 89 (2015) 332–343, https://doi.org/10.1016/j.porgcoat.2015.03.016.
[48] A. Amirudin, D. Thieny, Application of electrochemical impedance spectroscopy to study the degradation of polymer-coated metals, Prog. Org. Coat. 26 (1995) 1–28, https://doi.org/10.1016/0300-9440(95)00581-1.
[49] S. Martinez, B. Hudec, I. Šoić, Low-frequency EIS interpretation with the potential to predict the durability of protective coatings, Prog. Org. Coat. 197 (2024) 108811, https://doi.org/10.1016/j.porgcoat.2024.108811.
[50] E. Huttunen-Saarivirta, G.V. Vaganov, V.E. Yudin, J. Vuorinen, Characterization and corrosion protection properties of epoxy powder coatings containing nanoclays, Prog. Org. Coat. 76 (2013) 757–767, https://doi.org/10.1016/j.porgcoat.2013.01.005.
[51] C. Noè, L. Iannucci, S. Malburet, A. Graillot, S. Grassini, Vanillin-based Photocurable Anticorrosion Coatings Reinforced with Nanoclays, Macromol. Mater. Eng. 309 (2024) 2400155, https://doi.org/10.1002/mame.202400155.
[52] Z. Hussain, X. Wang, I. Riaz, Z. Lin, W. Nie, Y. Lin, C. Tao, Y. Huang, Experimental and multi-scale simulation evaluation of nanoclay/nanosilica epoxy coatings for enhanced corrosion protection of structural steel, Corros. Sci. 260 (2026) 113574, https://doi.org/10.1016/j.corsci.2025.113574.
[53] R.K. Bharadwaj, Modeling the Barrier Properties of Polymer-Layered Silicate Nanocomposites, Macromol 34 (2001) 9189–9192, https://doi.org/10.1021/ma010780b.
[54] A. Liguori, K.I. Garfias Gonzalez, M. Hakkarainen, Unexpected self-assembly of carbon dots during digital light processing 3D printing of vanillin Schiff-base resin, Polymer 283 (2023) 126252, https://doi.org/10.1016/j.polymer.2023.126252.